REPORT DOCUMENTATION PAGE

Form Approved
OMB No. 0704-0188

1. REPORT DATE *(DD-MM-YYYY)*	2. REPORT TYPE	3. DATES COVERED *(From - To)*
16-06-2011	Conference Paper	

4. TITLE AND SUBTITLE

Three-Dimensional Characterization of Polydisperse Particulate Composites from Microtomography

5a. CONTRACT NUMBER

5b. GRANT NUMBER

5c. PROGRAM ELEMENT NUMBER

6. AUTHOR(S)
Steven Atkinson

5d. PROJECT NUMBER

5f. WORK UNIT NUMBER
OSDB10TG

7. PERFORMING ORGANIZATION NAME(S) AND ADDRESS(ES)

IllinoisRocstar LLC
EnterpriseWorks Bldg.
60 Hazelwood Drive
P.O. Box 3001
Champaign, IL 61826-3001

8. PERFORMING ORGANIZATION REPORT NUMBER

AFRL-RZ-ED-TP-2011-243

9. SPONSORING / MONITORING AGENCY NAME(S) AND ADDRESS(ES)

Air Force Research Laboratory (AFMC)
AFRL/RZS
5 Pollux Drive
Edwards AFB CA 93524-7048

10. SPONSOR/MONITOR'S ACRONYM(S)

11. SPONSOR/MONITOR'S NUMBER(S)
AFRL-RZ-ED-TP-2011-243

12. DISTRIBUTION / AVAILABILITY STATEMENT

Approved for public release; distribution unlimited (PA #11265).

13. SUPPLEMENTARY NOTES
Undergraduate Thesis (Dept of Aerospace & Mechanical Engineering, University of Notre Dame.

14. ABSTRACT

This work contributes to a larger effort to analyze the mechanical and transport properties of polydisperse particulate composites. In order to improve the understanding of the morphology of such systems, specimens are analyzed from tomographic images. The material is first characterized by idealized shapes, and the representative pack is analyzed using high-order statistics in order to gain knowledge about the microstructure of the pack. Using this information, the effort proceeds by either constructing a representative unit cell (RUC) on which numerical analysis can be effectively performed, or performing computations using variational methods based on the statistical data to determine properties of interest. In this work, surrogate packs of rice, mustard, salt, and mixtures of rice and mustard are analyzed. Specimens are scanned using X-ray microtomography. A three-dimensional voxel pack is then reconstructed from the tomographic images. The voxel pack is analyzed in the image analysis software, Amira, to identify individual particles and their centroids, volumes, surface areas, and inertia tensors. Next, an algorithm is developed which reduces the particles of the voxel pack to ellipsoids or cuboids. Next, an algorithm is developed which reduces the particles of the voxel pack to ellipsoids or cuboids. An objective function is used to choose characteristic lengths of the idealized shapes to match the surface area and volume of the corresponding voxel particles.

15. SUBJECT TERMS

16. SECURITY CLASSIFICATION OF:			17. LIMITATION OF ABSTRACT	18. NUMBER OF PAGES	19a. NAME OF RESPONSIBLE PERSON
					Mr. William Harrigan
a. REPORT	b. ABSTRACT	c. THIS PAGE	SAR	82	19b. TELEPHONE NUMBER *(include area code)*
Unclassified	**Unclassified**	**Unclassified**			N/A

Three-Dimensional Characterization of Polydisperse Particulate Composites from Microtomography

An Undergraduate Thesis

Submitted to the Department of Aerospace and Mechanical Engineering
of the University of Notre Dame

by

Steven Atkinson,

_____

Karel Matouš, Director

Department of Aerospace and Mechnical Engineering
Notre Dame, Indiana
June 2011

Three-Dimensional Characterization of Polydisperse Particulate Composites from Microtomography

Abstract

by

Steven Atkinson

Heterogeneous materials are a useful class of materials that are used due to their properties in a diverse array of applications. However, detailed knowledge about these materials is still limited at present, and much can be learned if methods of analysis are improved.

This work contributes to a larger effort to analyze the mechanical and transport properties of polydisperse particulate composites. In order to improve the understanding of the morphology of such systems, specimens are analyzed from tomographic images. The material is first characterized by idealized shapes, and the representative pack is analyzed using high-order statistics in order to gain knowledge about the microstructure of the pack. Using this information, the effort proceeds by either constructing a representative unit cell (RUC) on which numerical analysis can be effectively performed, or performing computations using variational methods based on the statistical data to determine properties of interest.

In this work, surrogate packs of rice, mustard, salt, and mixtures of rice and mustard are analyzed. Specimens are scanned using X-ray microtomography. A three-dimensional voxel pack is then reconstructed from the tomographic images. The voxel pack is analyzed in the image analysis software, *Amira*, to identify individual particles and their centroids, volumes, surface areas, and inertia tensors. Next, an algorithm is developed which reduces the particles of the voxel pack to ellipsoids or cuboids. An objective function is used to choose characteristic lengths of the idealized shapes to match the surface area and volume of

the corresponding voxel particles. For ellipsoidal particles, the orientations of the representative shapes are found by minimizing certain norms between the geometric inertia tensor of the particles from the voxel pack (micro-CT data) and the geometric inertia tensor of the corresponding representative ellipsoid. For cuboids, the orientation of the particle feret length and width are matched, and the best of the two resulting possible orientations is chosen through a comparison of the particles' inertia tensors.

The representative particles' size and shape are characterized using geometric metrics. An optimization algorithm is developed which creates two discrete, two-dimensional probability density functions (pdf's) of the particles based on the metrics: one with a high number of subdivisions (raw micro-CT data), and a second with an optimized number of subdivisions (representative pack data). The number and spatial position of the bins of the latter (coarse) discretization are optimized to mimic the fine experimental data.

Lastly, one-, two-, and three-point probability functions are computed on the pack in order to gather statistical data about its morphology, using the modes assigned to the particles from the optimized coarse binning. Future efforts may utilize this statistical information in order to compute upper and lower bounds for mechanical and transport properties using the Hashin-Shtrikman variational methods.

CONTENTS

CHAPTER 1

Introduction

It has long been known that the microstructures of heterogeneous materials are intimately linked to their overall macroscopic behavior [1, 2]. Moreover, it has been a problem of great interest to use microstructural data in order to inform models which attempt to describe these overall properties. One subset of materials which presents unique challenges is that of heterogeneous materials.

A subset of heterogeneous materials–particulate composites–may be characterized by the packing of its particle inclusions. This packing may be random and difficult to characterize. In fact, these packing problems are very pervasive and are applicable to a range of disciplines. On the molecular level, the analysis of packing leads to information about molecular structure in a number of classes of matter, including granular metals, glasses, and liquids [3, 4]. In addition, the packing behavior of nanoparticles is of crucial importance to their performance in a variety of applications [5]. On a higher length scale, packing analysis can be applied to cases such as sand and sedimentary rocks, pills in a bottle of medicine, packages of food, or coins in a jar [6–9].

In many of these aforementioned examples, properties of interest such as elastic modulus, ultimate strength, thermal conductivity, permeability, or process behavior are dependent on the properties of individual inclusions as well as the packing behavior of the aggregate system [2, 10]. Characteristics such as the ordering (or lack thereof) of inclusions, presence of voids or impurities, and the relative concentrations of the constituent phases in a material all have drastic implications for the response of the overall composite. Moreover, it is known that

heterogeneous mixtures of materials can lead to the development of mechanical and transport properties which are often nonlinear and also very often more desirable than those of a single component. Examples of this are abundant, including metallic alloys, fiber-reinforced plastics such as fiberglass, and steel-reinforced concrete found in roads and buildings, to name a few.

The general structure of random packs of particulate systems is a very complex topic. Definitions have been put forth to differentiate between loose-packed, close-packed, and ordered (crystalline) packing behaviors, and rigorous mathematical quantification of such systems is currently of interest [11]. Therefore, efforts have been made to develop computational processes to generate systems of randomly packed particles of various shapes [12–16]. At the same time, the development of x-ray tomography has allowed for non-destructive *in situ* observation of real heterogeneous media [17]. Moreover, the data-rich quantification of pack morphologies afforded by x-ray tomography can serve to experimentally validate the behavior of the computational efforts of packing codes.

In the Computational Physics Group at the University of Notre Dame, methods have been established for processing tomographic data in order to identify and quantify geometrical properties of individual spherical particles in a pack, and computational routines have been demonstrated which fit idealized shapes to voxel particles through the minimization of objective functions based on the particles' geometrical properties [18, 19]. The distribution of types of particles has been quantified on the basis of particle diameter. Statistical descriptors have been used which quantify the geometrical properties of particulate packs through the use of one-, two-, and three-point correlation functions.

Building on this past work, the contributions of this thesis are:

- Experimental data about particulate specimens was acquired using micro-computed tomography. Test cases of rice, black mustard, and salt inclusions are used to demonstrate the methods. Distinct modes of polydisperse mixtures of rice and black mustard have been identified and distinguished on the basis of particles' average grayscale intensity in a reconstructed voxel image set.
- Algorithms were developed which convert discrete voxel data about a particle into a representative ellipsoid or cuboid. An adaptive method may also be used which compares these two shapes and determines which representation possesses the lowest error.

- A binning algorithm was developed which characterizes the distribution of particles in a pack in terms of size and shape, using metrics which define particles' representative "pseudo-diameter" and eccentricity, respectively.
- A legacy code, *Stat3D* was advanced in order to numerically evaluate one-, two-, and three-point probability functions on packs of ellipsoidal particles.
- A routine was written for *Stat3D* which incorporates an assumption of semi-isotropy to compute three-point probability functions at a substantially lower computational cost.

The computational resources developed are used in the current work to quantitatively describe the changes in morphological characteristics for a collection of polydisperse particulate systems. The changes in morphology, shown through first-, second-, and third order statistical data, showcase the complex interactions which give rise to the noteworthy properties of heterogeneous mixtures.

Future work on the subject includes the use of the statistical information about the pack in tandem with stochastic methods in order to derive mechanical and transport properties using higher-order statistics [20]. In addition, other particle shapes may be considered to develop a more extensive library of shapes, allowing for the proper characterization of packs which feature a greater diversity of inclusions. The use of idealized shapes may be validated through the computation of the statistical descriptors on tomographically-derived voxel packs, and the computation of mechanical and transport properties through statistical methods may be validated through physical experimentation.

CHAPTER 2

Micro-Computed Tomography

In order to obtain data to be analyzed, specimens were prepared which were scanned in a micro-CT, including packs of rice, mustard, and salt to serve as surrogate systems which readily exhibit packing behavior associated with ellipsoids, spheres, and cuboids, respectively. The use of real particulate systems assures that the packing behavior of the system is realistic and incorporates all associated real-world phenomena. Past work has been done which uses packing algorithms which generates packs of particles, though such codes fail to capture all of the packing behavior which occurs in a real specimen [14]. However, more recent developments in experimental techniques using microtomography have allowed for non-invasive analysis of particulate packs in order to determine basic information about the constituent particles of a pack [21]. The current chapter explains the methods involved in acquiring and processing the tomographic data from a particulate pack.

In order to illustrate the concepts described throughout the following methodology, two particulate packs will be used. The first is a pack of long-grain white rice (shown in Figure 2.1) which shows how the methods apply to packs of ellipsoidal particles, and the second is a pack of salt (shown in Figure 2.2) which shows the applications to cuboidal particles.

2.1 Specimen Preparation

An example specimen of rice is shown in Figure 2.1. In order to prepare the specimen, the following procedure was followed:

- A cylindrical canister was used with a diameter of 6.2 cm and height of 6.5 cm to fit in the scanning chamber of the micro-CT.

Figure 2.1. A sample of long-grain white rice. Grains were loaded into the cylindrical canister, and the canister was tapped on the table until the rice appeared to have settled.

- Rice was poured into the container until it was filled nearly to the brim of the container.
- The container was tapped on a table until the rice particles had settled (indicated when the level of the rice in the container stopped descending). This criterion is assessed qualitatively during preparation and confirmed later quantitatively through investigation of the specimen's packing fraction.
- The container was mounted to the testing stage of the Micro-CT using Sticky Tack and tightened into place in the Micro-CT.

For spherical particles such as black mustard, an extra step was employed in which particles were rolled down an inclined plane. Particles which are more spherical tend to roll more quickly, while irregular particles tend to have trouble rolling, and do not make it to the bottom of the plane, allowing for the particles to be filtered with respect to sphericity. This was important in preparing the polydisperse packs that are discussed in chapter 5.

Packs of salt were also prepared and scanned. Due to the smaller particle size, the salt was prepared in a 7 mm plastic drinking straw. The straw was cut to length (about 3 cm) and one end of the straw was closed off by gluing a small piece of paper to its end. The rest of the preparation was carried out in a matter similar to the procedure described above. The prepared sample is shown in Figure 2.2.

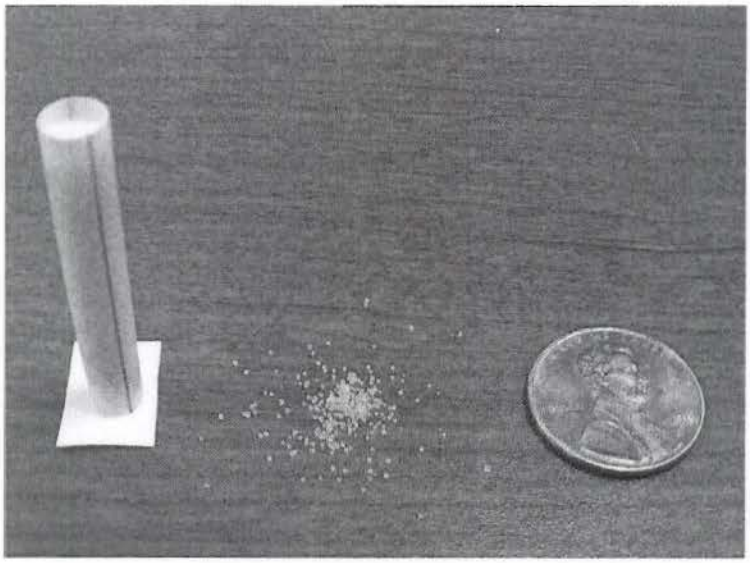

Figure 2.2. A prepared sample of salt.

2.2 Micro-CT System

The tomographic scanner used in this work is a Skyscan 1172 high-resolution Micro-CT, shown in Figure 2.3. The basic principle of its operation is illustrated in Figure 2.4. The micro-CT functions by emitting x-rays from a source towards a specimen with a camera on the other side. Because the specimen's constituent phases vary in density, they absorb different amounts of x-ray radiation; a particle with a higher density possesses more material which the x-ray must pass through in a given volume, in which a greater quantity of x-ray radiation is absorbed. X-ray scattering effects also occur which affect the characteristics of the x-ray radiation after interacting with the surfaces of inclusions. These effects combine to give unique signatures which are linked to distinct phases in the pack A correlation between grayscale intensity and material density may be constructed based on the application of Beer's law, though it is sufficient for the goals of the current work to note that different phases may readily be identified by differences in x-ray interactions [22].

The resulting pattern of x-ray intensity that is detected by the camera is what constitutes the monochromatic tomographic images, such as the example shown in Figure 2.5(a). After

a tomographic projection is taken, the specimen is rotated incrementally by a given value $\Delta\theta$ while the camera and source remain stationary, resulting in a new projection of the sample. The process of image acquisition and specimen rotation is repeated until the resulting image set contains tomographic cross-sections of the specimen through a full 360° of rotation. By decreasing $\Delta\theta$, the clarity of the reconstructed image set (discussed in Section 2.3) is increased. In the current work, an incremental rotation of $\Delta\theta = 0.15°$ was used.

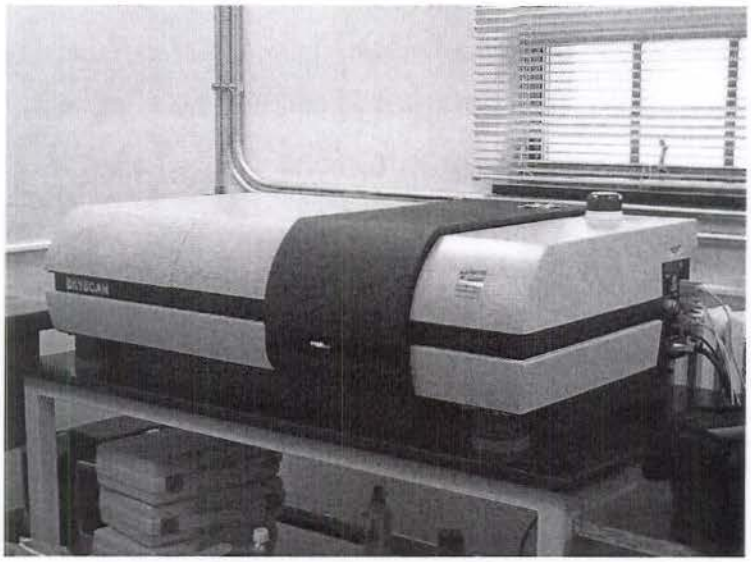

Figure 2.3. The Skyscan 1172 high-resolution Micro-CT scanner which was used to obtain microtomographic data on particulate packs.

2.3 Post-Processing of Tomographic Image Sets

After the tomographic image set has been acquired from the micro-CT, a number of post-processing steps are taken to convert the x-ray images to a binary three-dimensional voxel pack on which analysis will take place.

A commercial program, *NRecon*, is used to construct a three-dimensional voxel image of the specimen using the tomographic cross-sections [23]. The voxel image is stored as a collection of horizontal cross-sectional slices. The basic concept of this conversion is shown in Figure 2.6. It is important to notice that the tomographic cross-sections differ by a rotational

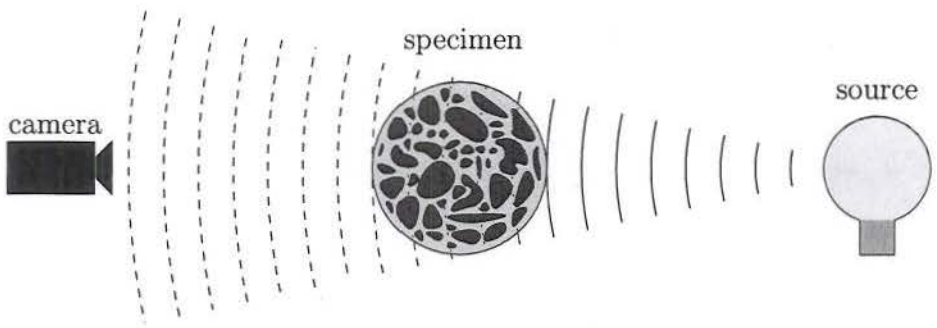

Figure 2.4. The basic layout of the micro-CT's main components. A source emits x-rays towards a specimen, and the radiation is detected by a camera on the other side, which takes tomographic images.

increment, while the reconstructed cross-sections differ by a translational increment, meaning that the tomographic images contain different views of the same part of the specimen, while the reconstructed cross-sections each contain information that does not overlap. In addition, the reconstruction algorithm may be carried out in parallel since the image set may be divided and evaluated with minimal overlap of data (see Figure 2.5 for an example of a single tomographic cross-section and horizontal constructed slice).

After the grayscale voxel pack has been constructed, the image set must be filtered and post-processed in order to retrieve the meaningful information about the pack. In order to do this, *Amira*, a commercial software package, is used to apply a series of filters on the three-dimensional image set and visualize the voxel pack [24].

The first filter that is applied is an edge-preserving smoothing filter. The filter works by diffusing differences in intensity (grayscale value) through the image set. In order to preserve edges where the intensity changes rapidly (indicating the boundary of a particle or other surface), diffusion is prevented from crossing large gradients. The results of edge-preserving smoothing are shown for a single cross-section in Figure 2.7.

The second filter to be applied is a thresholding filter. This filter converts the image set

(a) A tomographic cross-section of close-packed long-grain white rice.

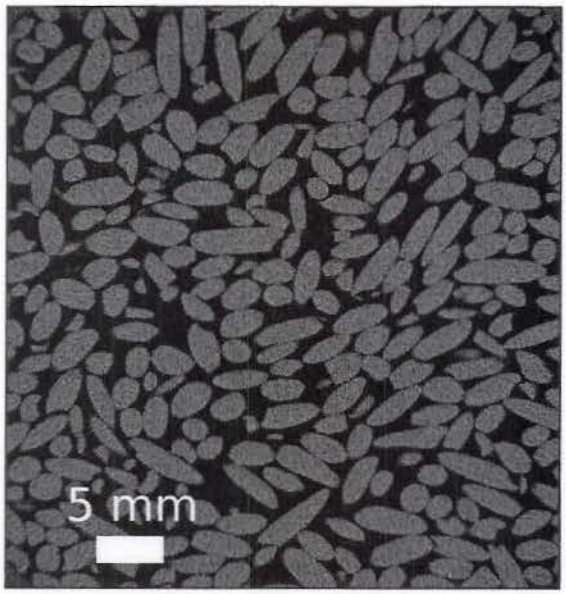

(b) A reconstructed horizontal cross-section of the pack.

Figure 2.5. A collection of tomographic images such as the one shown in (a) are reconstructed to create a three-dimensional voxel pack, composed of horizontal cross-sectional images such as the one in (b).

from a grayscale image to a binary image, evaluating the binary value of every voxel, $\tilde{\rho}_i$ to

$$\tilde{\rho}_i = \begin{cases} 1 \text{ if } \rho_{min} \leq \rho_i \leq \rho_{max} \\ 0 \text{ otherwise,} \end{cases} \tag{2.1}$$

where ρ_i is the 8-bit grayscale intensity of a given voxel, and ρ_{min} and ρ_{max} are user-specified thresholding limits. The result of thresholding is shown in Figure 2.8.

Next, a hole-filling algorithm is employed. Since the thresholding algorithm operates on a point-by-point basis and the density of the particles varies throughout, thresholding introduces voids inside particles where $\rho_i < \rho_{min}$. The filter proceeds iteratively, progressively

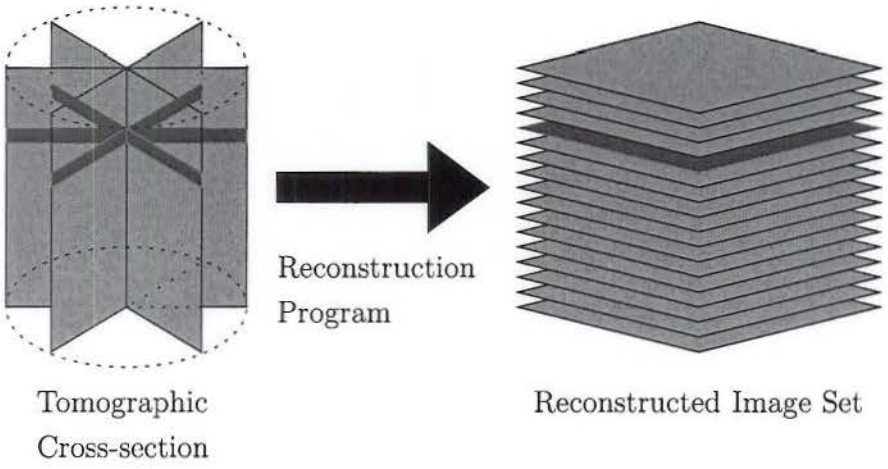

Figure 2.6. The reconstruction process. *NRecon* converts the tomographic cross-sections (left) into a three-dimensional voxel pack, composed of horizontal cross-sections. Parallelization is carried out by dividing the tomographic image set into sections (such as the one shown in red) that may be processed independently.

filling in holes, using one of three user-specified connectivity criteria that requires the voxel in question to be surrounded on either 6, 18, or 26 positions, as shown in Figure 2.9. Depending on the criterion chosen, the filter will either fill in more (6-point criterion) or less void space (26-point criterion) according to what is defined as sufficiently "inside" the inclusion. Since it was assumed that all particles are completely solid and have no hollow cavities, the 6-point connectivity criterion was used because of its more liberal results. Due to the quality of this particular scan, not many voids exist in the voxel pack, and the effects of the filter are subtle.

After the holes have been filled, a separating algorithm is applied in which the contact points between particles are identified and voxels are removed in order to segment the particles into disconnected entities. While *Amira's* algorithm for separation works well for concave shapes such as spheres and ellipsoids (see Figure 2.10), it does not perform as well for cuboids. Therefore, an erosion filter was used to separate cuboids, and a dilation algorithm was subsequently implemented in order to recover the lost material while making sure that gaps were not re-joined. The drawback to this method is that particles which are smaller than a minimum size (determined by the amount of erosion used) are completely lost, and

Figure 2.7. A cross-section of the voxel pack after smoothing. Notice that the particles have a constant density throughout in contrast to the variation seen in Figure 2.5(b).

Figure 2.8. The cross-section of the voxel pack after thresholding.

the shapes of the remaining particles were slightly distorted due to the assumptions that must be made in dilation. For example, a particle that has been eroded down to a single voxel might assume the form of a cube or a sphere depending on the type of dilation that is employed. Moreover, the orientation of such a particle is completely lost, since a single-voxel particle has no intrinsic orientation. This leads to a degree of uncertainty in the analysis of cuboid packs, and the distortion due to this separation algorithm can be seen in Figure 2.11.

Since voxels are removed from the image set in order to separate particles, a corresponding error is introduced in the pack's volume fraction. However, when the voxel size is small

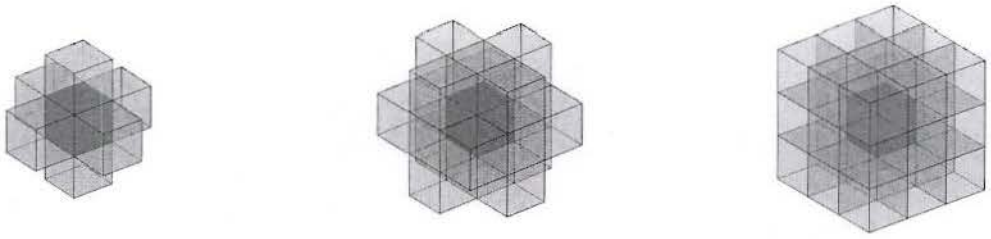

(a) 6-point connectivity (b) 18-point connectivity (c) 26-point connectivity

Figure 2.9. The different options for evaluating the connectivity of a given voxel. The 6-point definition (figure (a)) is the most relaxed choice and causes the most liberal hole-filling, while the 26-point definition (figure (c)) requires the most complete surroundings and yields more conservative results.

compared to the sizes of the inclusions, this error is also small. The changes in volume fraction due to separation are quantified in tables 2.1 and 2.2 for the rice and salt packs, respectively.

Figure 2.10. The cross-section of the voxel pack after *Amira's* separation filter.

After individual particles have been separated, the last filter to be applied is a border kill, in which particles that are touching the outside faces of the pack are deleted. This is done since such particles are only partially included in the voxel pack, and therefore, their shape does not reflect their true geometrical form. The results of the border kill for the rice pack are shown along with the rest of the filtering process for comparison in Figure 2.12. More

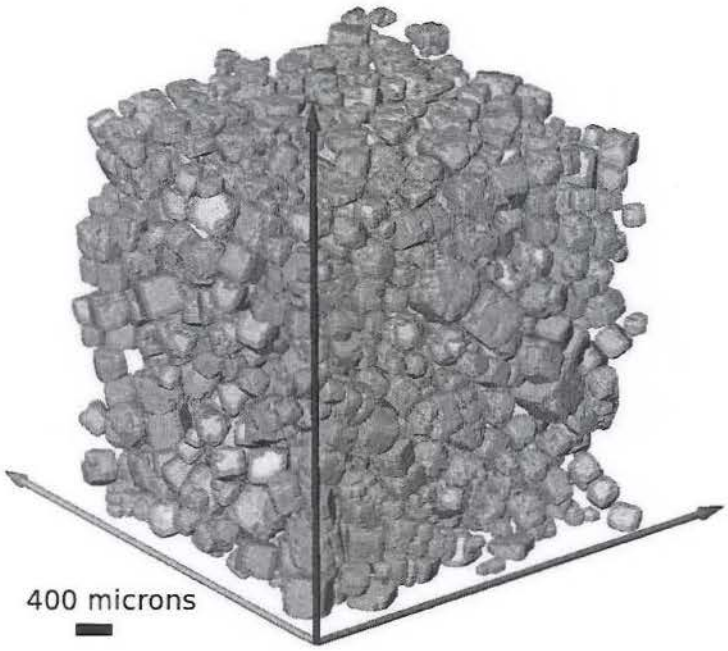

Figure 2.11. The voxel pack of a packed salt specimen. Notice that the edges of the particles have been smoothed and some particle definition has been lost due to the separation process required to identify individual particles.

technical details on the aforementioned filtering algorithms can be found in the program's instructional manuals [24, 25].

Since some partial particle information has been purposefully omitted through the border kill operation, the bounds of the pack domain must be adjusted accordingly so that the void space that has been introduced is not considered during analysis. This problem will be addressed in section 3.1. The scan data after filtering for the rice and salt packs are shown in tables 2.1 and 2.2, respectively.

Though there are multiple sources of error which are encountered through the post-processing procedure, the two sources of error which may be readily quantified and treated are the incremental rotation during image acquisition, $\Delta\theta$; and pixel resolution. First, $\Delta\theta$ was decreased until its contribution to the error in the image set was small compared to the other sources of error. Using this value of $\Delta\theta$, the effects of pixel resolution were studied. A tradeoff exists between pack detail through fine resolution and dataset size. This tradeoff becomes problematic when the dataset becomes too large for *Amira* to process (no similar problems were encountered due to the size of the tomographic projection images while decreasing $\Delta\theta$ and using *NRecon* to reconstruct three-dimensional image sets). Therefore, an investigation was conducted in which a pack of rice was scanned at multiple resolutions, using $\Delta\theta = 0.15°$. The resulting voxel packs were post-processed, and the volume fraction of the particles was determined. The results are shown in Figure 2.13. Based on the results of the investigation, all subsequent analyses of rice and mustard packs were carried out with a resolution of 64.9 μm.

After the post-processing of the voxel pack has been completed, analysis can be carried out in order to characterize particles in the pack. In order to do this, an analysis tool is used in *Amira* which quantifies several properties of interest for each particle:

- volume, V_{CT}
- surface area, S_{CT}
- centroid location, $(\bar{x}, \bar{y}, \bar{z})$
- second moments of area, M_{xx}, M_{yy}, and M_{zz}

- product moments of area, M_{xy}, M_{xz}, and M_{yz}
- maximum and minimum feret diameters; l and w, respectively (cuboids only)
- azimuthal and zenithal orientation of maximum and minimum feret diameters: θ_l, ϕ_l, θ_w, and ϕ_w (cuboids only).

Note that the second moments and product moments of area may be manipulated to generate a purely geometrical analog of the particle's inertia tensor. The definitions for the moments that *Amira* computes are

$$M_{xx} = \frac{1}{V_{CT}} \sum_{\omega} (x_i - \bar{x})^2 , \tag{2.2}$$

$$M_{yy} = \frac{1}{V_{CT}} \sum_{\omega} (y_i - \bar{y})^2 , \tag{2.3}$$

$$M_{zz} = \frac{1}{V_{CT}} \sum_{\omega} (y_i - \bar{z})^2 , \tag{2.4}$$

$$M_{xy} = \frac{1}{V_{CT}} \sum_{\omega} (x_i - \bar{x})(y_i - \bar{y}) , \tag{2.5}$$

$$M_{yz} = \frac{1}{V_{CT}} \sum_{\omega} (y_i - \bar{y})(z_i - \bar{z}) , \tag{2.6}$$

$$M_{xz} = \frac{1}{V_{CT}} \sum_{\omega} (x_i - \bar{x})(z_i - \bar{z}) , \tag{2.7}$$

where x_i, y_i, and z_i are the x-, y-, and z-coordinates of a voxel inside the inclusion domain, ω. These quantities may be used to form the particle's geometric inertia tensor:

$$\mathbf{I}_{CT} = V_{CT} \begin{bmatrix} M_{yy} + M_{zz} & -M_{xy} & -M_{xz} \\ -M_{xy} & M_{xx} + M_{zz} & -M_{yz} \\ -M_{xz} & -M_{yz} & M_{xx} + M_{yy} \end{bmatrix} . \tag{2.8}$$

This geometrical inertia tensor differs from a conventional inertia tensor in that the density of the inclusion is assumed constant and equal to 1. The result is a metric which may be used to describe the shape and orientation of the particle.

Table 2.1

Scan data and image processing data for the rice pack.

Pixel Size	69.40	μm / pixel
Volume of interest	$619 \times 656 \times 714$	pixel^3
	2.90×10^8	voxels
	$4.30 \times 4.55 \times 4.96$	cm^3
	96.91	cm^3
Bounding box	$3.84 \times 4.09 \times 4.48$	cm^3
	70.18	cm^3
Volume fraction before separation	0.6735	
Volume fraction after separation	0.6552	
Percent of volume remaining	97.28	%
Decrease in overall volume fraction	0.0183	
Number of particles before boundary layer removal	5968	
Number of particles after boundary layer removal	4040	

Table 2.2

Scan data and image processing data for the salt pack.

Pixel Size	3.986	μm / pixel
Volume of interest	$944 \times 944 \times 962$	pixel^3
	9.57×10^8	voxels
	$3.76 \times 3.76 \times 3.83$	mm^3
	54.15	mm^3
Bounding box	$3.38 \times 3.38 \times 3.45$	mm^3
	39.41	mm^3
Volume fraction before separation	0.6322	
Volume fraction after separation	0.4656	
Percent of volume remaining	73.65	%
Decrease in overall volume fraction	0.1666	
Number of particles before boundary layer removal	1660	
Number of particles after boundary layer removal	1283	

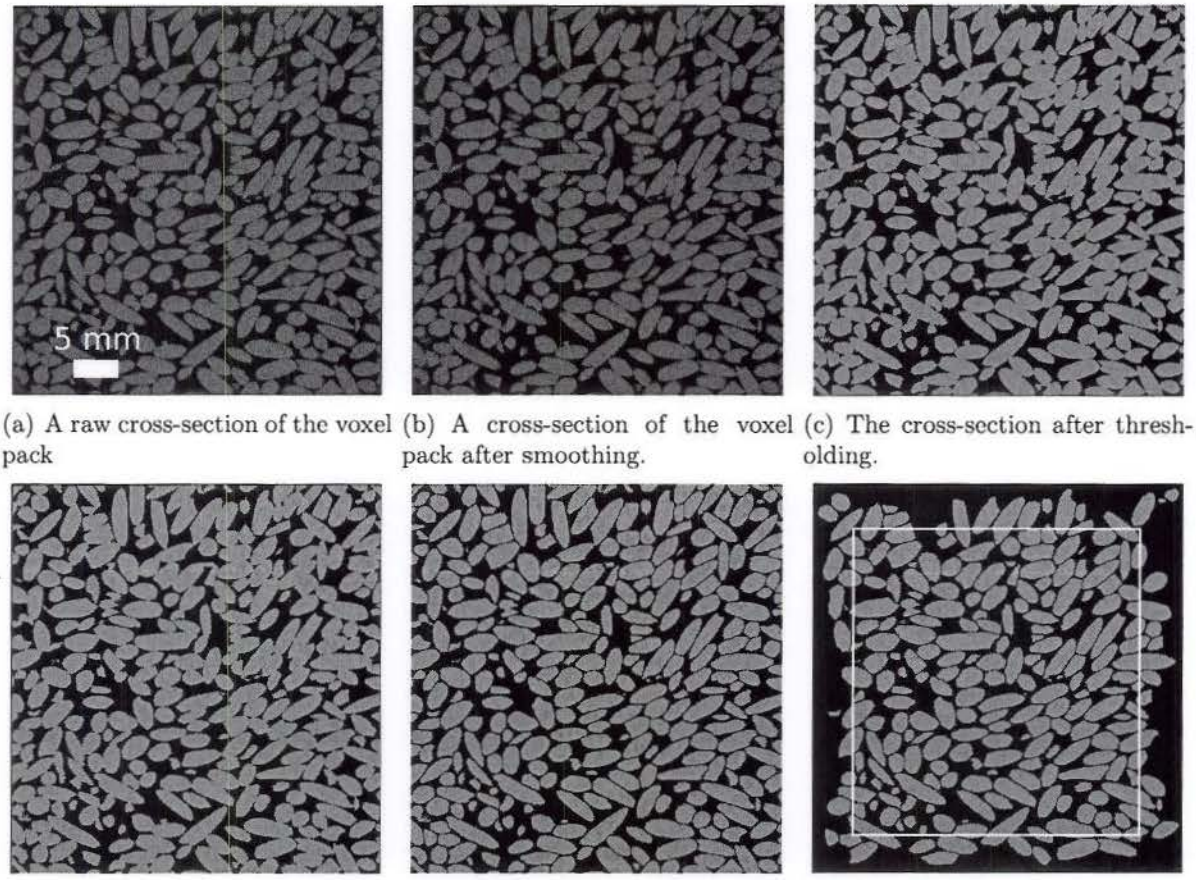

(a) A raw cross-section of the voxel pack

(b) A cross-section of the voxel pack after smoothing.

(c) The cross-section after thresholding.

(d) The cross-section after hole-filling.

(e) The cross-section after separation.

(f) The cross-section with border particles removed.

Figure 2.12. The effects of the various filters to the voxel pack, shown for a single cross-section. The raw grayscale images such as the one shown in (a) are smoothed (shown in (b)), then thresholded (shown in (c)) in order to create a binary image. Next, the hole-filling filter (shown in (d)) corrects any voids that are inside particles. Due to the quality of this particular scan, not many voids exist in the voxel pack, and the effects of the filter are subtle. Next, the separation filter (shown in (e)) conditions the images in order to isolate the individual solid particles. Finally, particles which touch the border of the image (and therefore might be incomplete) are removed in the border kill algorithm. The final voxel pack which will be analyzed is shown in (f). Note also that, since particles have been removed from the border, the volume of interest is shrunk in order to maintain the proper volume fractions. This new border is shown as a white line. The determination of this new border is discussed in section 3.1.

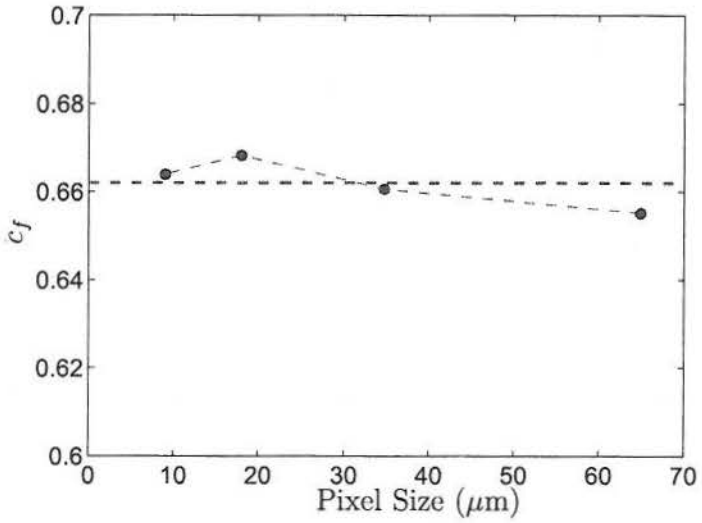

Figure 2.13. The volume fraction of the the rice pack for different scan resolutions after post-processing. It can be seen that the volume fraction of the pack is stable for all of the pixel sizes shown, so a 64.9 μm pixel size will be used in order to keep the data requirements to a minimum.

CHAPTER 3

Topology of Microstructure

After information has been gathered about the particles found in the voxel pack representation of the system, methods were developed to create a representative "pack" in which ideal geometrical shapes are chosen to approximate the characteristics of individual particles. Idealized representative particles present a number of advantages over the voxel particles:

- They represent a drastic savings in data size over the voxel pack.
- Their characteristics (such as size and shape) may be quantified in a more streamlined way than the voxel particles.

The current work focuses on the use of ellipsoidal and cuboidal particles to represent different particle shapes. In order to illustrate the procedures used, the rice and salt packs introduced in the previous section (tables 2.1 and 2.2) will be used, respectively.

3.1 Characterization of Individual Particles

The first step is to find a representation for an individual particle in terms of idealized shapes. Previous work has used spheres to represent voxel-based particles [18]. Spheres are effective and they provide a simple particle approximation if the orientation of the particle is unimportant or negligible. However, ellipsoidal particles present several distinct advantages:

- A wider variety of particle shapes may be accounted for through adjusting the aspect ratio of the ellipsoid.
- Ellipsoids have a quantifiable orientation, given by the orientation of their three semi-axes.

The first representative shape which will be discussed is an ellipsoid. Ellipsoids possess six degrees of freedom (three semiaxes and a unique 3-dimensional orientation) which must be minimized in order to best fit a given voxel particle. In order to pick values for the various properties of the ellipsoid, two objective functions are minimized independently.

In order to formulate a first guess at the lengths of the semiaxes of the equivalent ellipsoid for a given particle, the geometric inertia tensor of the voxel particle, $\mathbf{I}_{CT}$ is diagonalized, and the resulting principal geometric moments of inertia, $I_{1,CT}$, $I_{2,CT}$, and $I_{3,CT}$ are used to compute an initial guess for the semiaxes:

$$a^* = \sqrt{\frac{C}{V_{ct}}(I_{1,CT} + I_{2,CT} - I_{3,CT})}, \tag{3.1}$$

$$b^* = \sqrt{\frac{C}{V_{ct}}(I_{1,CT} - I_{2,CT} + I_{3,CT})}, \tag{3.2}$$

$$c^* = \sqrt{\frac{C}{V_{ct}}(-I_{1,CT} + I_{2,CT} + I_{3,CT})}, \tag{3.3}$$

where a^*, b^*, and c^* are the initial guesses for the semiaxes (ellipsoid) or edge half-lengths (cuboid) of the particle, and C is a geometric coefficient. For ellipsoids, $C = 5/2$. However, the same method may be used to find the half-lengths of a representative cuboid. In this case, $C = 3/2$. These constants are derived from the definitions of the principal geometric moments of inertia for the respective particles. Since the principal geometric moments of inertia are ordered such that $I_{1,CT} \geq I_{2,CT} \geq I_{3,CT}$, it follows that $a^* \geq b^* \geq c^*$.

After the initial guess has been computed, information about the voxel particle's volume, V_{CT}, and surface area, S_{CT} are used to determine the size of the ellipsoid through the objective function

$$\mathrm{II}_1(k) = \eta \frac{V_{CT} - k^3 V_p^*}{V_{CT}} + (1 - \eta) \frac{S_{CT} - k^2 S_p^*}{S_{CT}}, \tag{3.4}$$

where η is an empirically-chosen weighting value (between 0 and 1) which balances the emphasis on fitting either volume ($\eta = 1$) or surface area ($\eta = 0$), k is a scaling coefficient to be optimized, and V_p^* and S_p^* are the volume and surface area of the representative particle based on the initial guesses a^*, b^*, and c^*. Note that the degree of k reflects the

dimensionality of the property which it is scaling (k^3 for volume in the first term, and k^2 for area in the second term). Recall that V_{CT} and S_{CT} were computed through analysis of the voxel pack in *Amira*. For the present work, a value of $\eta = 0.8$ was chosen. This results in a more rigorous matching of particle volume and a more relaxed emphasis on surface area. This choice to match the volume of the particles was made because the voxel image of a particle is inherently more accurate at capturing its volume than its surface area due to the interpolation and approximations which are necessary to capture the surface characteristics of a digital image [26]. The minimization of this objective function yields an optimal value of k which is used to compute the final dimensions of the particle:

$$\begin{Bmatrix} a \\ b \\ c \end{Bmatrix} = k \begin{Bmatrix} a^* \\ b^* \\ c^* \end{Bmatrix}. \tag{3.5}$$

Using the final dimensions, V_p and S_p, are computed:

$$V_p = \frac{4}{3}\pi abc, \tag{3.6}$$

$$S_p = 4\pi \left(\frac{(ab)^{p_e} + (ac)^{p_e} + (bc)^{p_e}}{3} \right)^{1/p_e}, \tag{3.7}$$

where $p_e = 1.6075$. The formula used to compute the surface area is an approximation known as Knud Thomson's formula [27].

Because the representative particle is chosen to best match an irregular shape, there are errors associated with the dimensions of the shape chosen. The error in volume and surface area are defined, respectively, as

$$\delta V = \left| \frac{V_{CT} - V_p}{V_{CT}} \right| \times 100\,[\%], \tag{3.8}$$

$$\delta S = \left| \frac{S_{CT} - S_p}{S_{CT}} \right| \times 100\,[\%]. \tag{3.9}$$

The distribution of errors for the reduction of the rice pack are shown in Figure 3.1. The choice of $\eta = 0.8$ manifests itself in these error quantifications by causing δV to be significantly smaller than δS.

After the dimensions of the shape have been determined, the orientation of the representative particle is determined. For ellipsoidal particles, this is found through a comparison of the geometric inertia tensors of the voxel particle, $\mathbf{I}_{CT}$, and the representative ellipsoid, $\mathbf{I}_p$. A second objective function is defined as

$$\Pi_2(\alpha,\beta,\gamma) = \frac{||\mathbf{I}_{CT} - \mathbf{A}(\alpha)\mathbf{B}(\beta)\mathbf{C}(\gamma)\mathbf{I}_p\mathbf{C}^{-1}(\gamma)\mathbf{B}^{-1}(\beta)\mathbf{A}^{-1}(\alpha)||_{\mathcal{F}}}{||\mathbf{I}_{CT}||_{\mathcal{F}}}, \tag{3.10}$$

where the subscript $\mathcal{F}$ denotes the Frobenius norm, defined on an arbitrary $m \times n$ matrix Ξ as

$$\|\Xi\|_{\mathcal{F}} = \sqrt{\sum_{i=1}^{m}\sum_{j=1}^{n}|\xi_{ij}|^2}, \tag{3.11}$$

and $\mathbf{A}(\alpha)$, $\mathbf{B}(\beta)$, and $\mathbf{C}(\gamma)$ are matrices which denote rotations of angles α, β, and γ about the x-, y-, and z-axes, respectively:

$$\mathbf{A}(\alpha) = \begin{bmatrix} 1 & 0 & 0 \\ 0 & \cos\alpha & -\sin\alpha \\ 0 & \sin\alpha & \cos\alpha \end{bmatrix}, \tag{3.12}$$

$$\mathbf{B}(\beta) = \begin{bmatrix} \cos\beta & 0 & \sin\beta \\ 0 & 1 & 0 \\ -\sin\beta & 0 & \cos\beta \end{bmatrix}, \tag{3.13}$$

$$\mathbf{C}(\gamma) = \begin{bmatrix} \cos\gamma & -\sin\gamma & 0 \\ \sin\gamma & \cos\gamma & 0 \\ 0 & 0 & 1 \end{bmatrix}. \tag{3.14}$$

Therefore, it can be seen that the proper selection of α, β, and γ leads to an orientation of the representative particle's inertia tensor which mimics that of the voxel particle's inertia tensor. The distribution of values for Π_2 for the rice pack are shown in Figure 3.1(c). Note that, while the distribution has a low average, there are some exceptions with substantially higher values. These cases correspond to instances where the separation algorithm described in section 2.3 failed to separate several inclusions. An example of a group of particles which was not fully separated is shown in Figure 3.2.

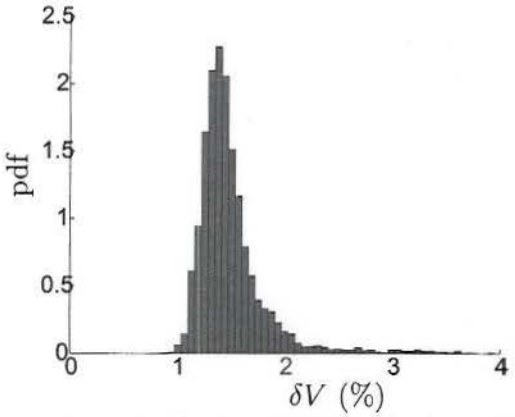

(a) The distribution of δV for the rice pack.

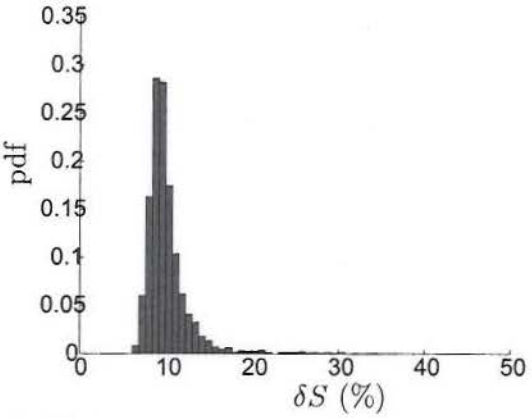

(b) The distribution of δS for the rice pack.

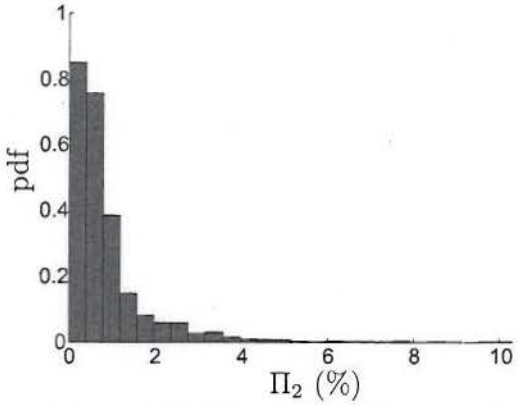

(c) The distribution of Π_2 for the rice pack.

Figure 3.1. Distributions of error for the particles in the rice pack for a weighting value $\eta = 0.8$. values of η closer to 0 drive δS to zero, while values approaching 1 drive δV to zero likewise. The low error suggests that rice particles are well-approximated by ellipsoids. While the mean value of Π_2 is low, the maximum value is substantially higher. This is because the separation algorithm used sometimes fails to properly separate particles, as is shown in Figure 3.2.

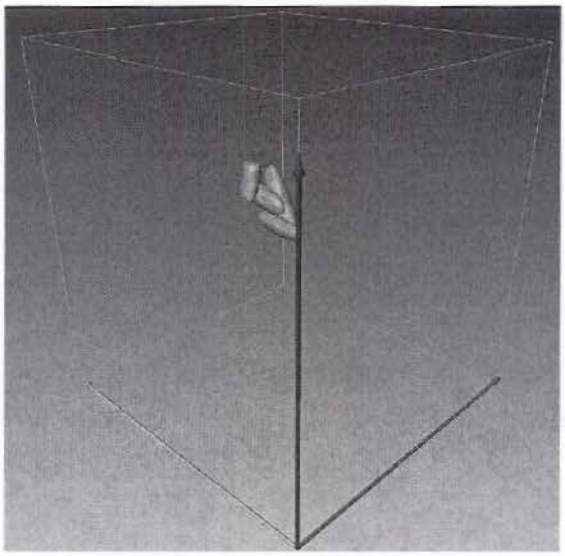

Figure 3.2. A group of particles which was not separated properly during the post-processing in *Amira*. Instances like this yield high values of Π_2 since an ellipsoid is not able to match the geometric inertia tensor of a complex shape such as this, causing a high difference between $\mathbf{I}_{CT}$ and $\mathbf{I}_p$.

However, for cuboidal particles, the use of the geometric inertia tensor is problematic because the geometric inertia tensor of a cube does not vary with orientation, and cuboids which are nearly cubic share this problem due to inaccuracies in the algorithms used to process the voxel data, most notably the crude separation methods which are responsible for the rounded edges seen in Figure 2.11. Therefore, an alternative method was chosen in which information about the voxel particle's feret length and width are computed and used to determine the orientation of the cuboid. It can be seen from Figure 3.3(a) that the maximum feret diameter, $\hat{l}$, of the cuboid spans the opposing corners of the particle, and the minimum feret diameter, $\hat{w}$, is parallel to the shortest edge of the particle. The orientation of these two diameters of the representative particle, $\hat{l}_p$ and $\hat{w}_p$ are rotated to match those of the voxel particle, $\hat{l}_{CT}$ and $\hat{w}_{CT}$. Finally, since these two vectors can denote two different orientations (shown in Figure 3.3(b)), the inertia tensors of the voxel particle and representative cuboid are compared using Π_2 for the two possible final orientations of

the cuboid. The orientation associated with the lower value of Π_2 of the two is selected as the final orientation of the cuboid.

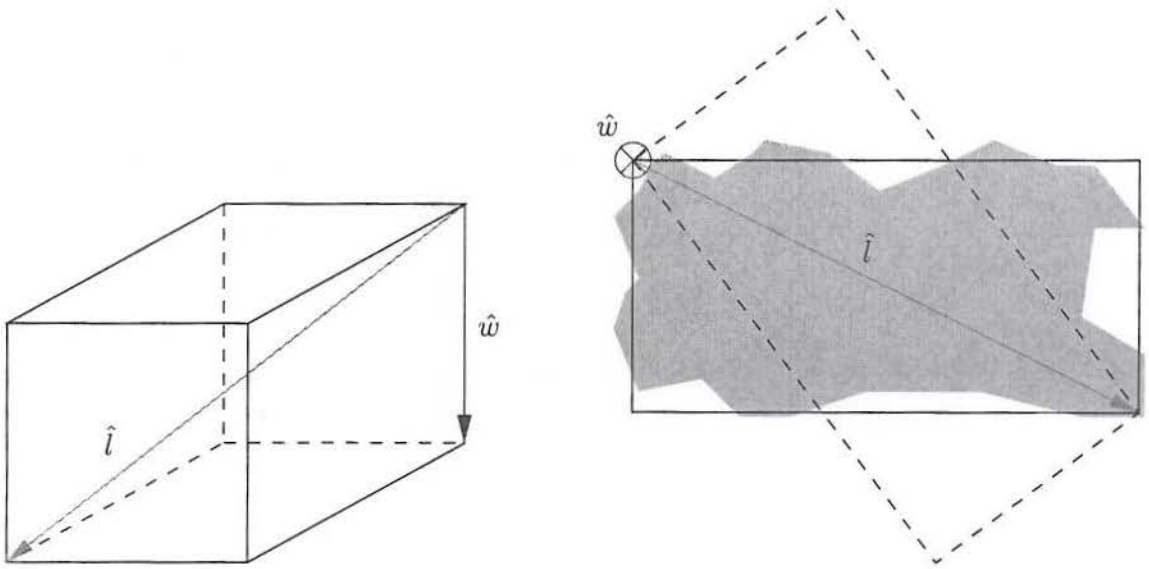

(a) The feret length $\hat{l}$ and width $\hat{w}$ of a cuboid. (b) The two possible orientations of a cuboid.

Figure 3.3. The pair of vectors used to quantify the orientation of the cuboid. The ideal cuboid (shown in (a)) is rotated until $\hat{l}$ and $\hat{w}$ are parallel to those of the voxel particle. The final choice between the two possible orientations (shown in (b)) is made based on a comparison of Pi_2 values associated with the two orientations.

The reduction process is carried out on every particle in the voxel pack, and the representative packs for the rice and salt packs are shown in figures 3.4 and 3.5. It can be seen in both these cases that the size, shape, and orientation of the voxel particles are accurately captured and represented in the respective idealized packs.

Recall that an important step in the voxel pack filtering described in section 2.3 was the removal of particles which were touching the boundary of the scanned volume of interest. Since the particles which were removed were replaced with open space, the volume of interest which will be considered must be resized. Since the voxel particles have now been characterized with representative idealized shapes, information can be used from the representative pack to inform the resizing of the volume of interest. In order to do this, twice the largest semiaxis (for ellipsoids), or the largest edge length (for cuboids) is found, and

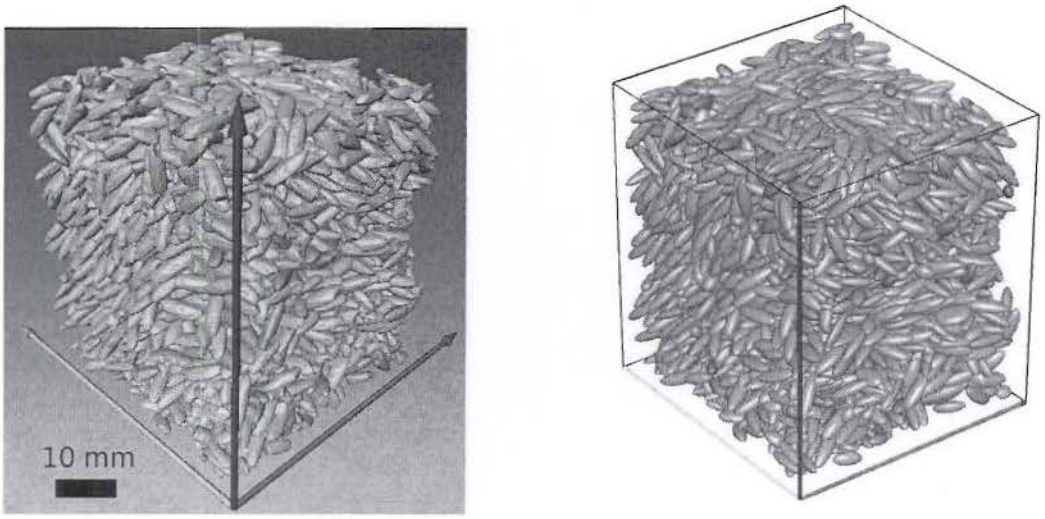

(a) The voxel pack for the rice sample.

(b) The equivalent ellipsoidal pack.

Figure 3.4. The voxel pack and equivalent ellipsoidal pack for the rice pack. Notice the one-to-one mapping of particles between the ellipsoidal pack and the voxel pack from which it is derived.

the volume of interest is decreased by an amount slightly larger than this quantity. This process is shown graphically in Figure 3.6. It is important to note that, while the volume of interest has been adjusted, no additional particles are explicitly eliminated beyond those affected by the border kill operation. The goal of this adjustment is to correctly capture the packing fraction of the pack. The particles that are cut by the new bounding window can be accurately characterized since their shape information is fully known.

3.2 Binning Algorithm

After a representative pack has been created, analysis may be performed on the collective distributions of particle types. Since the representative particles may have different sizes and shapes, geometric metrics were devised to quantify these two properties of the particles. The first property of a particle is its size, which is quantified by its pseudo-dimension, $\tilde{d}$. This is

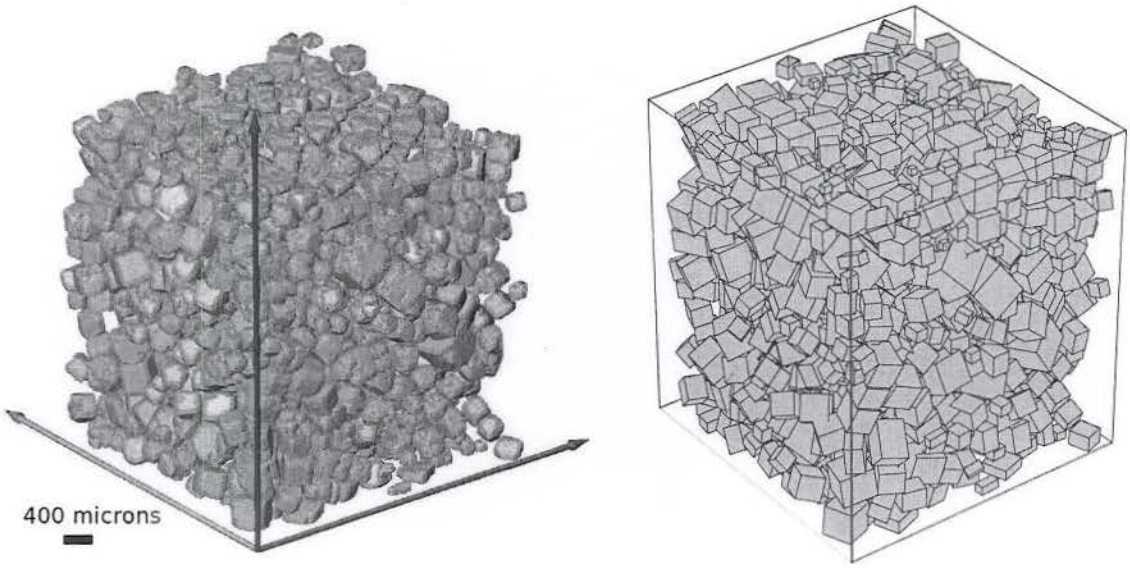

(a) The voxel pack for the salt sample.

(b) The equivalent cuboidal pack.

Figure 3.5. The voxel pack and equivalent cuboidal pack for the salt pack. Notice the one-to-one mapping of particles between the cuboidal pack and the voxel pack from which it is derived.

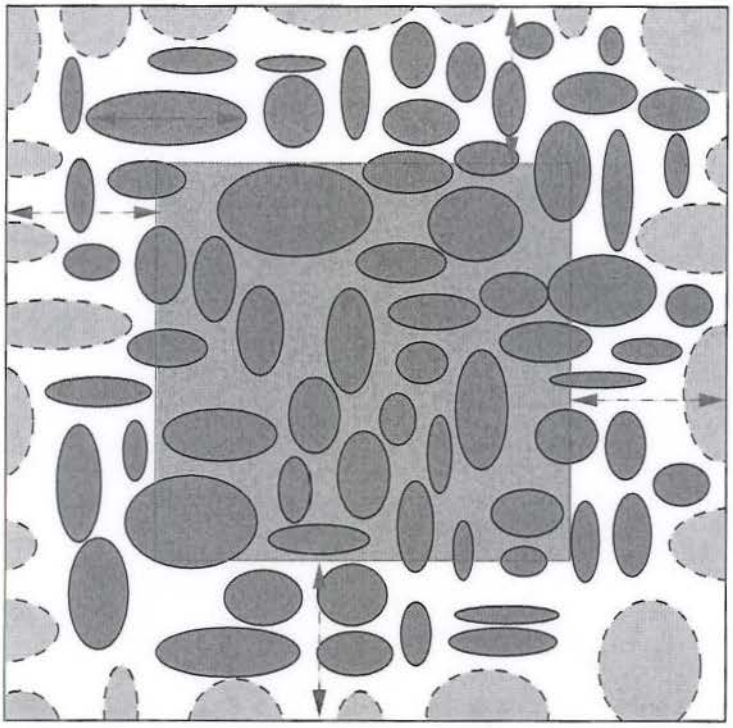

Figure 3.6. The process by which the volume of interest is resized, shown for a two-dimensional cross-section of the pack. After boundary particles (identified with a dashed boundary) have been removed by the border kill operation in the voxel pack, the volume of interest must be adjusted to obtain the actual volume fraction. First, the largest particle length is found (solid red arrow), then the volume of interest is shrunk on all sides by slightly more than this amount (dashed red arrows). The resulting volume of interest (light red area) contains no void space introduced by the border kill operation, and the overall volume fraction of the pack is preserved.

defined to be

$$\tilde{d} = \begin{cases} \left(\frac{9V}{\pi}\right)^{1/3}, & \text{for ellipsoids} \\ (V)^{1/3}, & \text{for cuboids} \end{cases} . \tag{3.15}$$

This parameter corresponds to the diameter of a sphere (for ellipsoids) or the side length of a cube (for cuboids) whose volume is equal to that of the representative particle in question. The second property of a particle is its shape. This is quantified using a metric ϵ, defined as

$$\epsilon = 1 - \frac{1}{3}\left(\frac{b}{a} + \frac{c}{b} + \frac{c}{a}\right). \tag{3.16}$$

Recall that, since $a \geq b \geq c$, it follows that ϵ is bounded between 0 (when $a = b = c$) and 1 (when $a \gg b \gg c$). With these metrics, a probability distribution function may be created for the pack in order to quantify the frequency of different sizes and shapes of its particles.

3.2.1 Uniform Binning

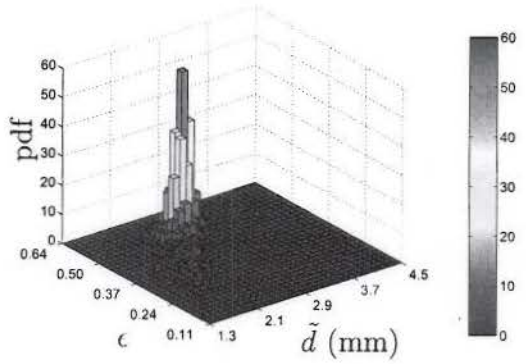

Figure 3.7. The fine binning of the rice pack. Details about the distribution of particle shapes and sizes are readily identifiable due to the fine mesh resolution.

First, a fine binning is created in which particles are binned into a quadrilateral mesh based on values of ϵ and $\tilde{d}$ from the voxel pack. Figure 3.7 shows a binning on a 40×40 quadrilateral mesh for the rice voxel pack. While this distribution shows a great amount of detail about the different types of particles found in the pack, it is desired to be able to classify the different particles in a relatively small number of bins while still capturing the

characteristics of the particle distribution. Therefore, a coarse binning is created in which fewer bins are used, and the difference between the coarse and fine binnings is quantified using a local error metric, defined as

$$\psi_{i_c} = \sum_{i_f=1}^{n_f} O_{i_c,i_f} \left| pdf_{CT}^{i_f} - pdf_p^{i_c} \right|, \tag{3.17}$$

where n_f is the number of bins in the fine discretization, O_{i_c,i_f} is the overlap between coarse bin i_c and fine bin i_f in the two-dimensional plane of the pdf, $pdf_{CT}^{i_f}$ if the probability density function associated with fine bin i_f, weighted by the volumes of the particles from the voxel pack; and $pdf_p^{i_c}$ is the probability density function associated with coarse bin i_c, weighted by the volumes of the particles from the ellipsoidal pack. By weighting the probability distribution by the volumes of the particles, the characteristics associated with the larger particles are accentuated, causing the contours of the probability distribution to be more pronounced. The effect is that the algorithm is forced to give greater weight to errors associated with large particles. This is desirable because there are often fewer large particles, yet their spatial characteristics define a large part of the geometrical configuration of the packing and therefore must be considered. The volume-weighted probability distribution for the fine binning is shown in Figure 3.8.

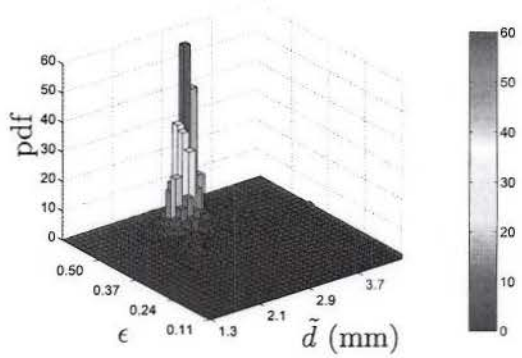

Figure 3.8. The volume-weighted probability density function for the fine binning. By weighting the probability density with the volume, more emphasis can be given to large particles which tend to occur less frequently in number than small particles.

3.2.2 Resizing

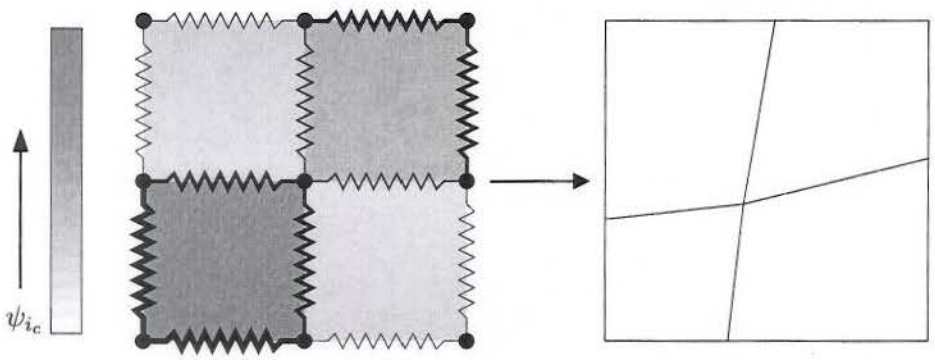

Figure 3.9. The spring analogy used to resize bins. Notice that springs have higher spring constants where the errors of the coarse bins are higher. This causes the bins with higher errors to shrink and gain resolution. Also notice the use of an "anchor" spring which is fixed to the original position of the node. This serves to relax the optimization method and prevent overcompensation.

A conditioning algorithm was formulated which employs several sequential algorithms to improve the coarse binning's characterization of the probability distribution. The first of these algorithms to be used is an iterative resizing algorithm. In every iteration, the algorithm first quantifies the local error in the coarse binning with respect to the fine binning, then resizes the bins in order to decrease the error until a minimum global error is achieved.

With information about the error associated with every bin, the vertices of the mesh are adjusted using a spring network analogy, shown in Figure 3.9. The edges of the bins are modeled as linear springs governed by Hooke's Law. They are joined at the nodes of the mesh, and outer nodes are constrained to remain on the border of the domain. The spring constants are determined by the errors associated with the bins which share the edge in question; the springs are stiffer when the bins sharing that edge have greater errors. In addition, an "anchor" spring is included at every node that is fixed to the original location of the node in order to prevent the nodes from moving too far in a single iteration. The algorithm iterates until the total error of the binning ceases to decrease. The result of the resizing algorithm on the rice pack is shown in Figure 3.10.

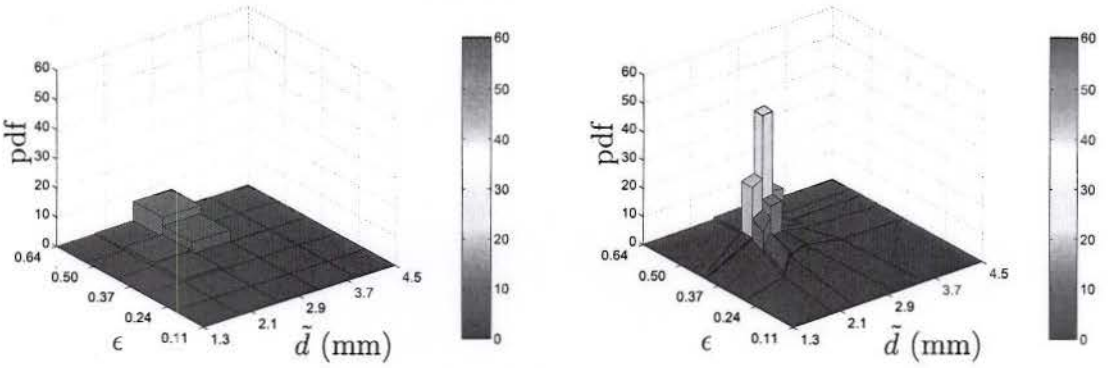

(a) The uniform binning of the rice pack.

(b) The resized binning of the rice pack.

Figure 3.10. The binning before (a) and after (b) resizing. Notice that, by changing the shape of the discretization, the binning captures the characteristics of the distribution much better.

3.2.3 Truncation

After the resizing algorithm has converged to a minimum error, the second conditioning algorithm is a truncation routine in which the sizes of bins on the outer rim of the probability distribution are identified and shrunk. Figure 3.11 shows a binning before and after the truncation algorithm. The particles, represented by dots, are used to define a border similar to a convex hull to which the bins may be shrunk, since the algorithm does not allow any points to fall outside of this binning domain.

3.2.4 Division

After truncation has been carried out, the next conditioning algorithm to be carried out is a division algorithm. The first part of this algorithm divides bins based on size; if a bin is too large, it may include particles which are drastically different in characteristics. For example, a bin which spans too great a range of values for ϵ may contain both spherical particles and very eccentric particles. Therefore, limits on the span of any given bin are imposed for both properties, and any bin which violates the limits is divided accordingly. In

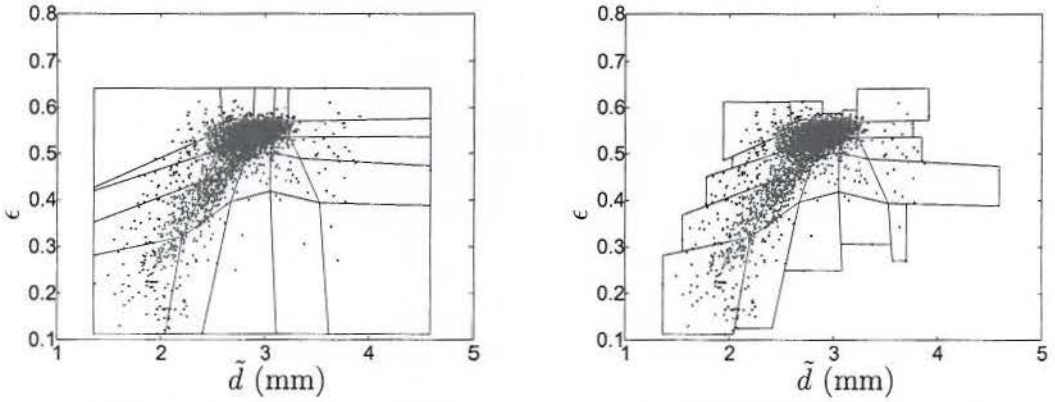

(a) The binning before truncation.

(b) The binning after truncation.

Figure 3.11. The effects of the truncation algorithm. The algorithm identifies bins which include the outside border of the binning domain, and shrinks them to fit the data more tightly.

the present work, the criteria which were empirically chosen are

$$\frac{\tilde{d}^i_{max} - \tilde{d}^i_{min}}{\tilde{d}_{max}} < 0.3, \tag{3.18}$$

$$\epsilon^i_{max} - \epsilon^i_{min} < 0.2, \tag{3.19}$$

where $\tilde{d}^i_{max}$ and $\tilde{d}^i_{min}$ are the maximum and minimum values of $\tilde{d}$ for coarse bin i, $\tilde{d}_{max}$ is the global maximum pseudo-diameter; and $\epsilon^i max$ and ϵ^i_{min} are the maximum and minimum eccentricities for coarse bin i. The results of the range-based division algorithm are shown in Figure 3.12.

Next, bins are identified which still possess a large local error ψ_{i_c} (See equation 3.17). Bins which possess the greatest local error are divided in order to reduce the local error in poorly-resolved areas. Division continues until either a maximum local error criterion is satisfied throughout the entire binning domain, or a predetermined maximum number of bins have been created. The results of error-based splitting are shown in Figure 3.13.

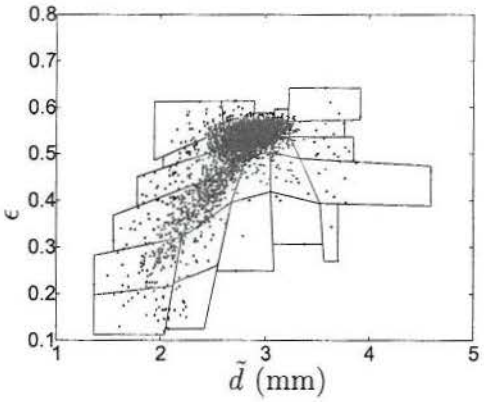

Figure 3.12. The binning after range-based splitting. Notice that the largest bins have been divided in order to decrease the variance of particle types which are included in a single bin.

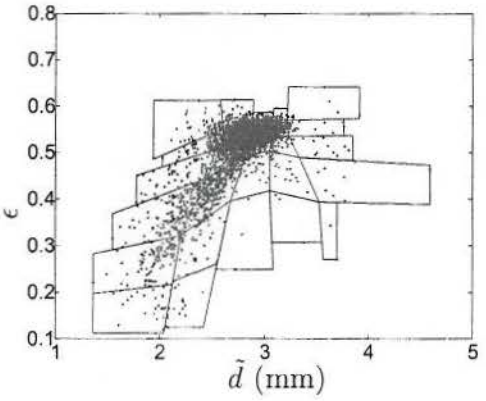

Figure 3.13. The effects of the error-based splitting algorithm. The algorithm identifies bins which possess the greatest local error, and splits them accordingly such that their error is reduced until either a criterion for maximum error or a maximum number of bins is satisfied.

3.2.5 Fusion

After division has been completed, a large number of bins may exist, and divisions may have been performed which do not improve the characteristics of the binning. In the first part of the process, pairs of neighboring bins are identified whose probabilities differ by less than within 10 % of the greatest probability and do not collectively span a larger range than the maximum criterion used in division. The investigation of the range and similar probability density ensures that any fusions carried out do not produce adverse effects to the error associated with the binning; by avoiding pairs of bins with large gradients in probability density, the global error of the binning is maintained while reducing the complexity of the binning.

The second part of the fusion routine searches for bins whose population does not meet a minimum requirement, defined for the current work as 10 particles. Bins which do not meet this requirement are fused with a neighboring bin. Selection is based upon the collective range of the pair; the smallest final pair is chosen to be fused. The results of the fusion routine are shown in Figure 3.14. The original fine binning is also included as a reference for comparison.

Using the binning scheme that has been developed, types of particles can be readily identified that correspond to distinct sizes and shapes. Figure 3.16 shows several different bins of representative particles along with the voxel pack particles from which they were derived. It can be seen that the separate bins provide a means to distinguish between particles of varying sizes and shapes, as was claimed.

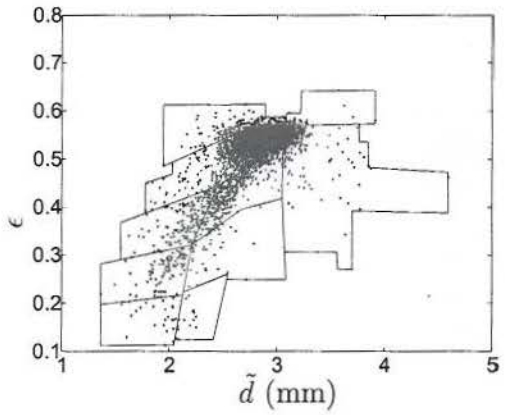

(a) The distribution of individual particles within the binning scheme.

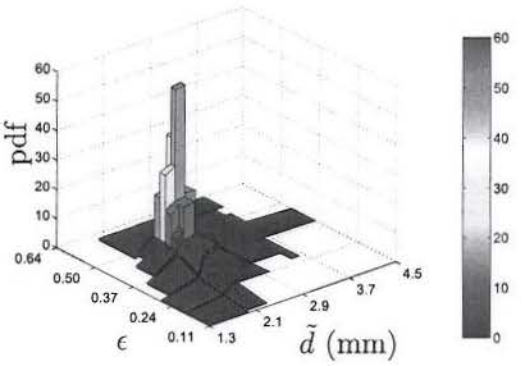

(b) The final coarse binning.

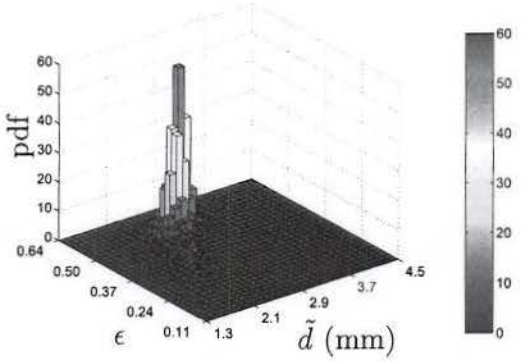

(c) The original fine binning.

Figure 3.14. The results of the fusion routine. Bins that were similar or whose population did not meet a minimum value were fused together with neighboring bins in order to reduce the number of bins while minimizing the amount of error reintroduced into the binning scheme. The fine binning is shown again in (c) for reference.

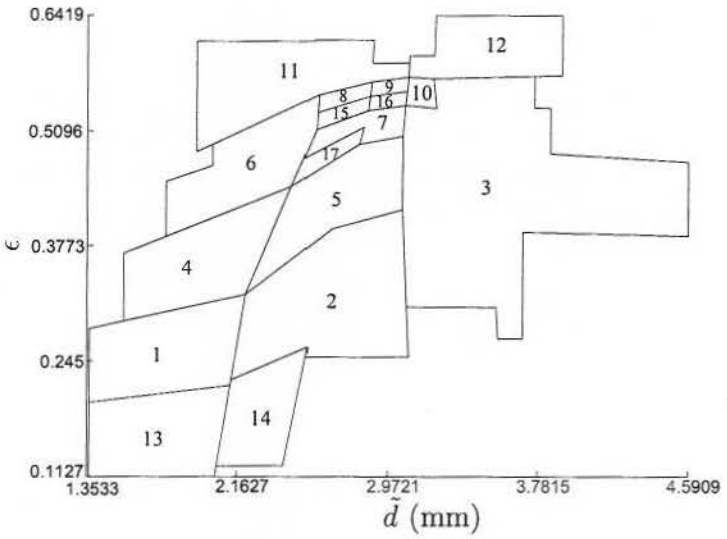

Figure 3.15. Indices associated with the coarse binning. Particles are assigned into different groups based on this discretization.

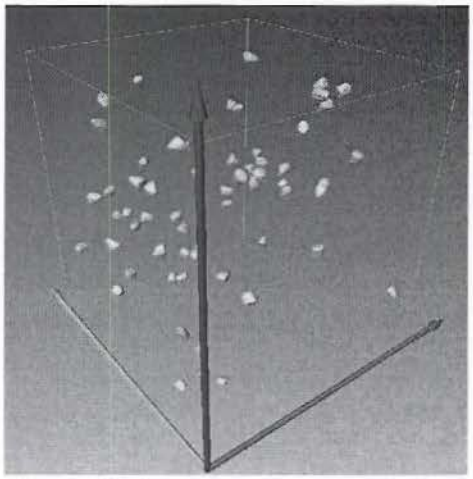

(a) Bin 1, voxel pack

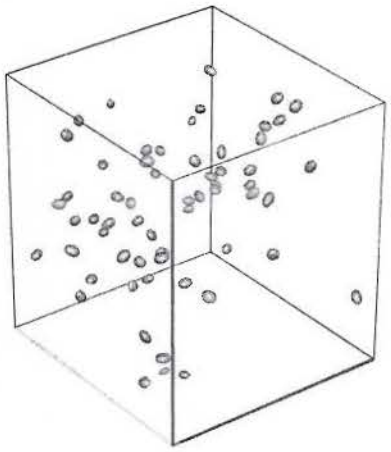

(b) Bin 1, equivalent ellipsoidal pack

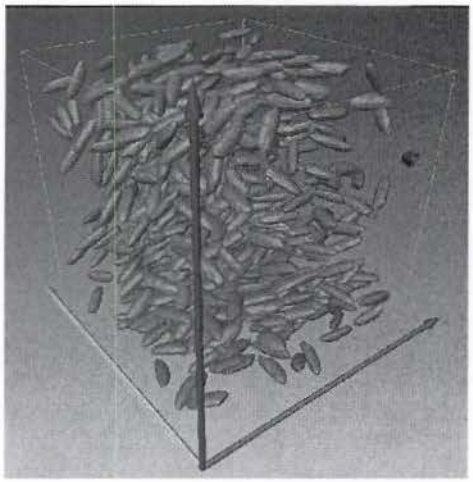

(c) Bin 15, voxel pack

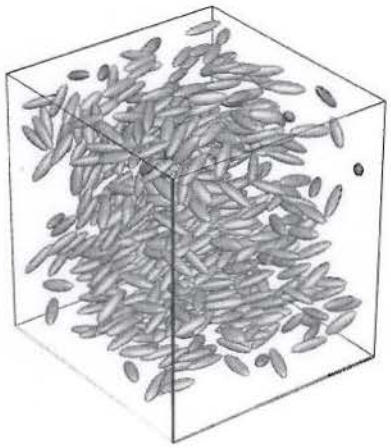

(d) Bin 15, equivalent ellipsoidal pack

Figure 3.16. Particles associated with several bins. Particles from the voxel pack are displayed beside their equivalent ellipsoids for the sake of comparison. Notice the one-to-one relation between the voxel particles and their ellipsoidal representations. Also notice that the particles from mode 1 (figures (a) and (b)) are small and more regular, while the particles from mode 15 are larger and more eccentric (figures (c) and (d)). Also note that bin 15 has the highest pdf associated with it (Figure 3.14(b)). This bin represents the "typical" grain of rice, which is reflected in the shape of the particles seen.

CHAPTER 4

Statistical Characterization

In order to characterize the morphology of the particulate microstructure, the statistical descriptors known as one-, two-, and three-point probability functions are used [2, 18]. In this chapter, the definitions of the n-point probability functions is reviewed for the sake of completeness, the numerical implementation of the functions is discussed, and the contributions of this work are identified and explained. In order to illustrate the statistics, selected probability functions are computed and shown for the rice pack from table 2.1.

4.1 Concept of Probability Functions

First, an indicator function, $\chi_r(\boldsymbol{x}, \omega)$ is defined to be

$$\chi_r(\boldsymbol{x}, \omega) = \begin{cases} 1 & \boldsymbol{x} \in D_r(\omega) \\ 0 & \text{otherwise,} \end{cases} \tag{4.1}$$

where $\boldsymbol{x}$ is a random point in the pack, ω is a particular ensemble member (eg. a scan of a specimen), and D_r represents the domain occupied by the r-th phase in ω. Using this function, the n-point probability function $S_{r_1,r_2,\ldots,r_n}$ may be computed, which states the probability of finding phases $r_1, r_2, \ldots, r_n$ simultaneously at points $\boldsymbol{x}_1, \boldsymbol{x}_2, \ldots, \boldsymbol{x}_n$ according to

$$S_{r_1,\ldots,r_n}(\boldsymbol{x}_1, \ldots, \boldsymbol{x}_n) = \overline{\chi_{r_1}(\boldsymbol{x}_1) \cdots \chi_{r_n}(\boldsymbol{x}_n)}, \tag{4.2}$$

where the overbar indicates the average over all ensemble members

$$\overline{\chi_r(\boldsymbol{x})} = \int_S \chi_r(\boldsymbol{x}, \omega)\, p(\omega)\, d\omega, \tag{4.3}$$

and $p(\omega)$ is the probability density of ω in the ensemble space $\mathcal{S}$. The ensemble space is defined as a collection of specimens which differ in morphological details, but share the same macroscopic characteristics (e.g., multiple scans of a rice pack). Then, $p(\omega)$ would be the probability density of a specimen in the ensemble $\mathcal{S}$.

The probability functions which will be evaluated in the current work include one-, two-, and three-point probability functions, which are shown as

$$S_r(\boldsymbol{x}) = \overline{\chi_r(\boldsymbol{x})}, \tag{4.4}$$

$$S_{r,s}(\boldsymbol{x}, \boldsymbol{x}') = \overline{\chi_r(\boldsymbol{x})\chi_s(\boldsymbol{x}')}, \tag{4.5}$$

$$S_{r,s,q}(\boldsymbol{x}, \boldsymbol{x}', \boldsymbol{x}'') = \overline{\chi_r(\boldsymbol{x})\chi_s(\boldsymbol{x}')\chi_q(\boldsymbol{x}'')}. \tag{4.6}$$

In special cases, the microstructure of the material in question may be simplified if it may be assumed that it is ergodic, homogeneous, and statistically isotropic [1]. These three assumptions correspond to ensemble member, translational, and directional independence of the n-point probability functions, respectively. If the first two assumptions are satisfied, equations 4.4, 4.5, and 4.6 reduce to

$$S_r(\boldsymbol{x}) \rightarrow c_r, \tag{4.7}$$

$$S_{r,s}(\boldsymbol{x}, \boldsymbol{x}') \rightarrow S_{r,s}(\boldsymbol{r}_1), \tag{4.8}$$

$$S_{r,s,q}(\boldsymbol{x}, \boldsymbol{x}', \boldsymbol{x}'') \rightarrow S_{r,s,q}(\boldsymbol{r}_1, \boldsymbol{r}_2), \tag{4.9}$$

where $\boldsymbol{r}_1 \equiv \boldsymbol{x}' - \boldsymbol{x}$ and $\boldsymbol{r}_2 \equiv \boldsymbol{x}'' - \boldsymbol{x}$. Furthermore, if the assumption of isotropy is satisfied as well, equations 4.8 and 4.9 reduce further to

$$S_{r,s}(\boldsymbol{r}_1) \rightarrow S_{r,s}(\|\boldsymbol{r}_1\|), \tag{4.10}$$

$$S_{r,s,q}(\boldsymbol{r}_1, \boldsymbol{r}_2) \rightarrow S_{r,s,q}(\|\boldsymbol{r}_1\|, \|\boldsymbol{r}_2\|), \tag{4.11}$$

where c_r is the volume fraction of phase r in the composite, $\|\boldsymbol{r}_1\|$ is the distance between points $\boldsymbol{x}'$ and $\boldsymbol{x}$, and $\|\boldsymbol{r}_2\|$ is the distance between points $\boldsymbol{x}''$ and $\boldsymbol{x}$.

In addition to these simplifying assumptions, there exist other special cases which are independent of pack morphology in which higher-order probability functions collapse to

lower-order cases when the points in question are either coincident or separated by a distance greater than the characteristic length of the pack, defined as the distance at which the values of the n-point probability functions converge to a constant value. They are

$$S_{r,s}(\boldsymbol{r}_1)\Big|_{\|\boldsymbol{r}_1\|\to 0} = c_r\delta_{r,s}, \tag{4.12}$$

$$S_{r,s}(\boldsymbol{r}_1)\Big|_{\|\boldsymbol{r}_1\|\to \infty} = c_r c_s, \tag{4.13}$$

$$S_{r,s,q}(\boldsymbol{r}_1,\boldsymbol{r}_2)\Big|_{\|\boldsymbol{r}_1\|\to 0,\ \|\boldsymbol{r}_2\|\to 0} = c_r\delta_{r,s}\delta_{r,q}, \tag{4.14}$$

$$S_{r,s,q}(\boldsymbol{r}_1,\boldsymbol{r}_2)\Big|_{\|\boldsymbol{r}_2\|\to 0} = S_{r,s}(\boldsymbol{r}_1)\,\delta_{s,q}, \tag{4.15}$$

$$S_{r,s,q}(\boldsymbol{r}_1,\boldsymbol{r}_2)\Big|_{\boldsymbol{r}_1=\boldsymbol{r}_2} = S_{r,s}(\|\boldsymbol{r}_1\|)\,\delta_{s,q}, \tag{4.16}$$

$$S_{r,s,q}(\boldsymbol{r}_1,\boldsymbol{r}_2)\Big|_{\|\boldsymbol{r}_1\|\to\infty,\ \|\boldsymbol{r}_2\|\to\infty} = c_r c_s c_q, \tag{4.17}$$

where $\delta_{i,j}$ is the Kronecker delta [2]. From these degenerate cases, it can be seen that the three-point probability functions contain various two- and one-point probability functions as subsets of their spaces.

Recall that the volume of interest was shrunk on the packs in Section 3.1. Through an investigation of the two-point probability functions, the characteristic length of the pack, l_c, may be determined as twice the distance at which the probability functions converge to the limit case in equation 4.13. Using this information, it is possible to conclude whether or not the size of the pack exceeds the minimum characteristic length needed for well-resolved statistics.

In the present work, n-point probability functions are used to determine correlation statistics between different bins (labeled for reference in figure 3.15) of particles in a pack. This allows for a more complete statistical characterization than if statistics are defined in terms of material phases only. However, this more complete characterization comes at an informational cost: whereas the simplest mode-based characterization requires $3^3 = 27$ different three-point probability functions for a complete third-order characterization of a three-phase medium, using a finer distinction between types of particles increases the statistical space drastically; for the rice pack, which consists of 17 bins and a matrix phase, there

are $(17+1)^3 = 5832$ possible three-point probability functions that must be computed in order to achieve a complete third-order statistical characterization of the pack. Thus, the goal to minimize the number of bins presented in chapter 3 becomes apparent.

Fortunately, several symmetric cases exist for two- and three-point probability functions which limit the number of independent functions that must be computed. Two simple examples which can be readily demonstrated are

$$S_{r,s}(\boldsymbol{r}_1) = S_{s,r}(-\boldsymbol{r}_1), \tag{4.18}$$

$$S_{r,s,q}(\boldsymbol{r}_1, \boldsymbol{r}_2) = S_{r,q,s}(\boldsymbol{r}_2, \boldsymbol{r}_1). \tag{4.19}$$

The general form of a single three-point probability function $S_{r,s,q}(\boldsymbol{r}_1, \boldsymbol{r}_2)$ spans a six-dimensional space, so a complete characterization of any single combination of r, s, and q is computationally expensive. Therefore, a simplifying assumption is made where the absolute direction of $\boldsymbol{r}_1$ and $\boldsymbol{r}_2$ are not considered. Instead, the angle between the two vectors, θ_{rsq} is used to quantify their directions relative to each other. This is the semi-isotropic assumption:

$$S_{r,s,q}(\boldsymbol{r}_1, \boldsymbol{r}_2) \rightarrow S_{r,s,q}(\|\boldsymbol{r}_1\|, \|\boldsymbol{r}_2\|, \theta_{rsq}). \tag{4.20}$$

This formulation of the three-point probability function is illustrated in figure 4.1. The semi-isotropic assumption collapses the statistical space of the three-point probability function from six dimensions to three, yielding significant savings in computational resources. In addition, all of the degenerate cases predicted for complete three-point probability functions are still observed. Another consequence of the semi-isotropic assumption is that there exists a special case for angles of $\theta_{r,s,q} > 180°$ which limits the number of angles that must be investigated. Namely, it is demonstrated that

$$S_{r,s,q}(\|\boldsymbol{r}_1\|, \|\boldsymbol{r}_2\|, \theta_{rsq}) = S_{r,s,q}(\|\boldsymbol{r}_1\|, \|\boldsymbol{r}_2\|, 2\pi - \theta_{rsq}). \tag{4.21}$$

This is due to the fact that, since the orientation of the plane described by points r, s, and q is assumed to be random, it is impossible to distinguish between these pairs of angles.

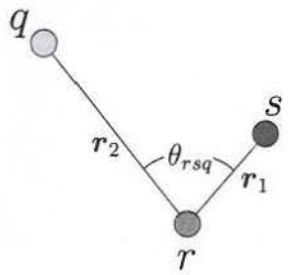

Figure 4.1. A general triple-throw used in computing a three-point probability function with the assumption of semi-isotropy. The indicator function is evaluated at r, s, and q, and the results are recorded as a function of $\boldsymbol{r}_1$, $\boldsymbol{r}_2$, and θ_{rsq}.

4.2 Numerical Implementation

While it is possible to evaluate the n-point probability functions in closed form for a variety of idealized particulate packs, it quickly becomes unrealistic to determine such solutions for complex microstructures such as those considered in the current work. Therefore, a numerical computation of the one-, two-, and three-point probability functions was developed.

A legacy program, *Stat3D*, which performs a numerical calculation of first-, second-, and third-order statistics of spherical particulate packs, was developed by the Computational Physics Group at the University of Notre Dame [19]. The general form of the program's execution is shown in figure 4.2. Its key features include:

- computation of one- and two-point probability functions, including isotropic two-point probability functions.
- a Monte Carlo-like sampling method using a sampling template shown in figure 4.3.
- a parallel implementation with linear speedup,

In the current work, several contributions were made to advance *Stat3D*:

- the program can compute a semi-isotropic three-point probability function with increased efficiency.
- the program can now compute all of the previously-stated probability functions on packs of ellipsoidal particles, such as those found in the rice pack.

By incorporating the semi-isotropic assumption into the numerical implementation of the three-point probability function *a priori*, a simplified sampling template, shown in figure

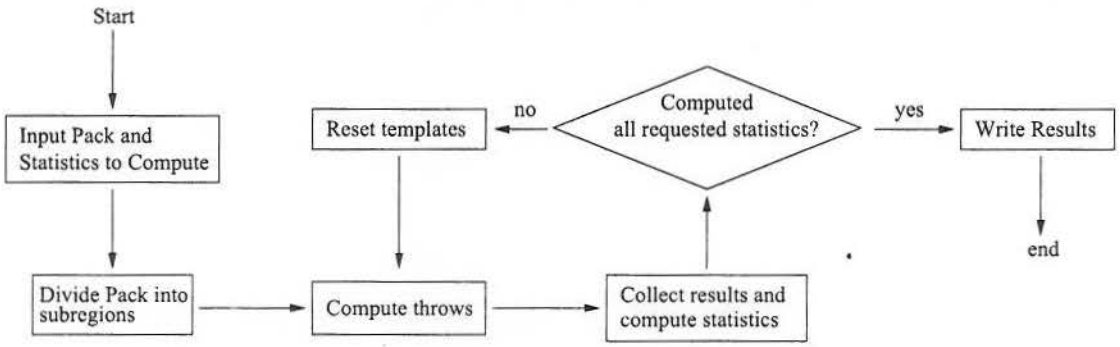

Figure 4.2. The layout of *Stat3D*. The program distributes information about the pack, statistics to be computed, and sampling template to all computing nodes which independently compute an equal portion of throws. The results of the individual nodes' statistical sampling is compiled on the master node, and the results are output for post-processing.

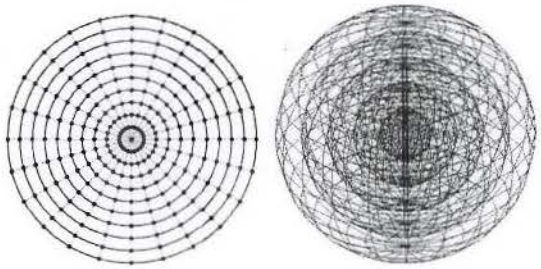

Figure 4.3. The template used in *Stat3D* to compute two-point probability functions. The template is composed of an array of sampling points spaced equally amongst n_r radial increments, n_θ azimuthal increments, and $\frac{n_\theta}{2}+1$ zenithal increments; in this example, $n_r = 5$ and $n_\theta = 20$. $\chi_r(\boldsymbol{x})$ is evaluated at the center point, and $\chi_s(\boldsymbol{x}')$ is evaluated at all of the surrounding points. The combination of both indicator functions yields equally-distributed statistical data for all directions which may be averaged to compute $S_{r,s}(\|\boldsymbol{r}_1\|)$ or used directly in computing $S_{r,s}(\boldsymbol{r}_1)$.

STAFF SUMMARY SHEET

	TO	ACTION	SIGNATURE (Surname), GRADE AND DATE		TO	ACTION	SIGNATURE (Surname), GRADE AND DATE
1	STINFO	Log in SS/ DT/Copy	K. Gfeller 21 Jun 2011 Technical Editor	6	S. Svejda	Review/ Approve	*Signed & Dated Approval Page AFRL Chief Technical Advisor
2	S. Svejda	Review/ Sign	*Signed & Dated Form 79 AFRL Chief Technical Advisor	7	STINFO	Update SS	[signature] Technical Editor 30 June 11
3	STINFO	Approval Page / SS	[signature] Technical Editor 22 June 11	8	D. Spotts	Review for PAO	Deborah A Spotts STINFO Officer 30 Jun 11
4	Darrell Rhoden	Review/ Approve	Darrell Rhoden OPSEC/FDO 29 June 11	9	J. Haire/M. Mingledorf	Review/ Clear	 Public Affairs Office
5	STINFO	Attach Rev Update SS	[signature] Technical Editor 30 June 11	10	STINFO	Notify/ Distribute	

SURNAME OF ACTION OFFICER AND GRADE	SYMBOL	PHONE	TYPIST'S INITIALS	SUSPENSE DATE
Kenette Gfeller	AFRL/RZOI	5-5016		20110621

SUBJECT	DATE
Undergrad Thesis: AFRL-RZ-ED-TP-2011-243 (Distribution A)	20110616

SUMMARY

STINFO DISTRIBUTION TEAM:

1. Please remember the spreadsheet (mark the date you took this document to each person on this route)
2. Please - NO PAPERCLIPS!

ALL:

1. Please review attached document
2. Mark any comments and sign your signature block on the attached "Authorization for Release"
3. Place document in your "out box" for pick-up and routing by a member of the Distribution Team

4.4, may be used. This allows the memory and speed characteristics for the evaluation of a $S_{r,s,q}(\|\boldsymbol{r}_1\|, \|\boldsymbol{r}_2\|, \theta_{rsq})$ to be of the same order as $S_{r,s}(\boldsymbol{r}_1)$.

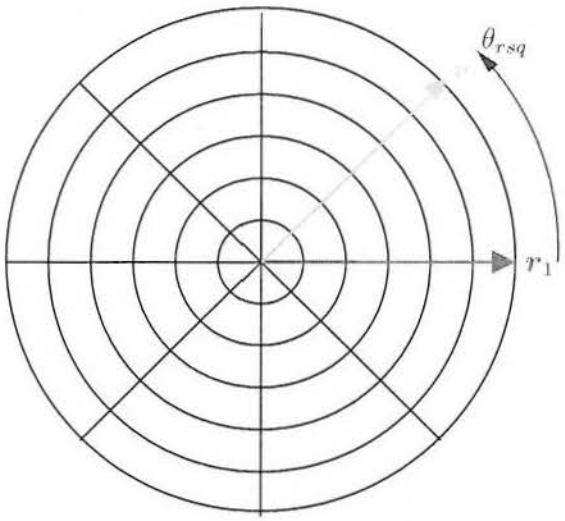

Figure 4.4. The template used to sample the pack for the new semi-isotropic third-order statistics routine. The template is given a random center point, then the direction of $\boldsymbol{r}_1$ is selected randomly. $\boldsymbol{r}_2$ then progresses around the circular planar template, which is rotated about $\boldsymbol{r}_1$ randomly, then $\chi_s(\boldsymbol{x}')$ and $\chi_q(\boldsymbol{x}'')$ are evaluated for all combinations of $\|\boldsymbol{r}_1\|$, $\|\boldsymbol{r}_2\|$, and θ_{rsq}.

Since the numerical implementation is based off of a finite number of samples, care must be taken to ensure that the number of template throws is great enough to ensure statistical convergence. Figure 4.5 shows the particle volume fraction as a function of the number of template throws for a contrived pack whose true volume fraction was computed in closed form. It can be seen that convergence has been achieved within an error of 0.74 % for $N_{throws} = 1,000,000$ template throws. This was then used as the minimum number of throws when computing all statistical information for the packs presented hereafter.

4.3 Numerical Examples

The results of statistical sampling of the rice pack are now presented in order to illustrate the various properties of the statistical descriptors used.

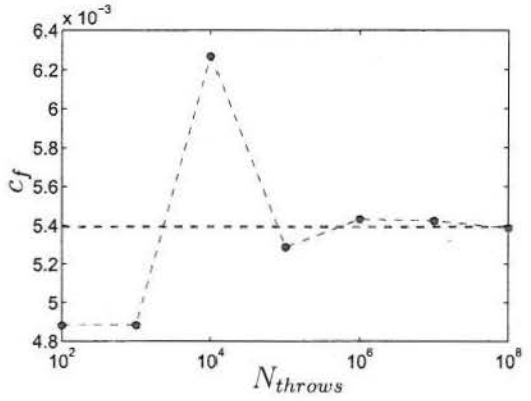

Figure 4.5. A convergence study conducted on a contrived pack using the particulate volume fraction as an indicator. The value has converged to an error of 0.74 % at $N_{throws} = 1,000,000$.

4.3.1 One-Point Probability Functions

It has already been shown that, when the assumption of ergodicity is satisfied, the one-point probability function $S_r(\boldsymbol{x})$ reduces to c_r, the volume fraction of bin r of the particles. Figure 4.6 shows the volume fractions of the individual bins of particles as derived from the voxel pack, as well as the volume fractions of the representative pack, as determined by statistical investigation.

4.3.2 Two-Point Probability Functions

The correlation of two points in two-point probability functions allows for spacial information to be quantified concerning the distribution of particles within the pack. When isotropy is assumed, the probability functions depend solely on the distance between the two points which are sampled (see figure 4.7). However, in a complete characterization, the probability is a function of direction as well (see figures 4.8 and 4.9). In the complete two-point probability distributions in figures 4.8(b), 4.8(c), a characteristic anisotropy can be seen when $\|\boldsymbol{r}_1\|$ is small. A closer investigation of the distribution of orientations of the particles reveals that the pack exhibits parallelity in which particles tend to lie flat and in

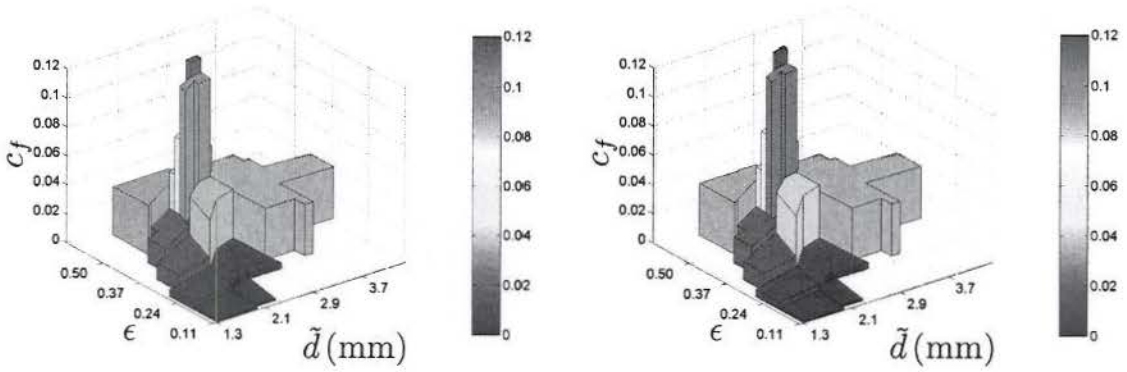

(a) Volume fractions derived from statistical sampling.

(b) Volume fractions derived from voxel-based particles from *Amira*.

Figure 4.6. One-point probability functions of the rice pack (shown in (a)). Notice that the values converge to the volume fractions of the subsets of representative ellipsoidal particles, which are similar to the volume fractions of the voxel particles which were derived from post-processing in *Amira* (shown in figure (b)). This is due to a low overall discrepancy in particle volumes, quantified by δV (see figure 3.1(a)), and convergence of the probability functions through a sufficiently high number of samples.

the same direction. This observation is validated through a quantification of particle orientations, shown in figure 4.10. In addition, as $\|\boldsymbol{r}_1\| \to 0$, these two-point probability functions converge to their respective degenerate cases that are predicted in equation 4.12. However, other two-point probability functions are highly anisotropic, as is shown in figures 4.9(a), 4.9(b), and 4.9(c). These selections demonstrate the very highly complex microstructure that arises from the random packing. Moreover, the specificity afforded by the binning allows the statistical descriptors to uncover these complex correlations that remain hidden when using more generic distinctions between types of inclusions (e.g., material phases only).

4.3.3 Three-Point Probability Functions

Lastly, three-point probability functions were computed for selected combinations of bins. Selected cases are shown in figure 4.11. The degenerate cases predicted in equations 4.15 and 4.16 are also shown as red dashed lines. In addition, the symmetry described in equation 4.19 and the angle identity described in equation 4.21 are shown in figures 4.12 and 4.13.

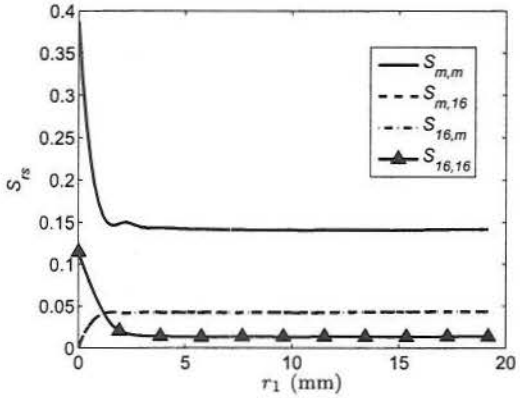

(a) Selected isotropic two-point probability functions performed on the rice pack.

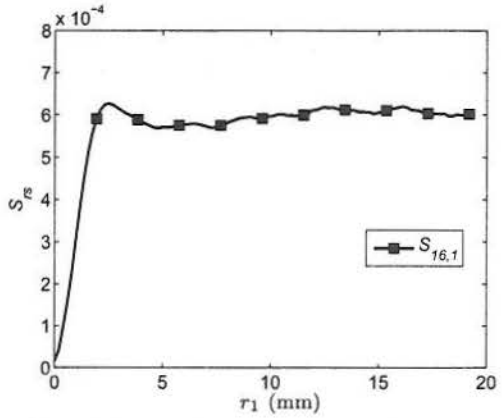

(b) Selected isotropic two-point probability functions performed on the rice pack (continued).

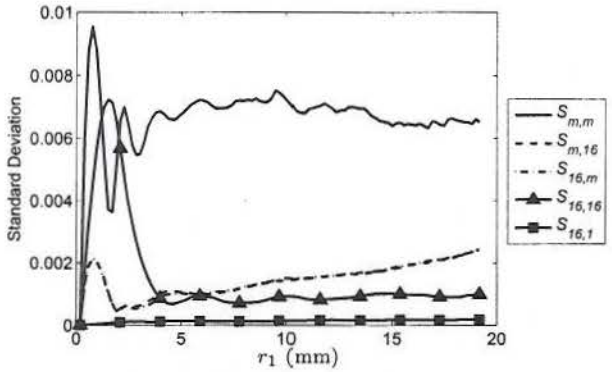

(c) The standard deviations of the isotropic two-point probability functions.

Figure 4.7. Selected two-point probability functions for the rice pack. Note that the functions converge to their respective one-point probability functions, $S_r\delta_{r,s}$ at $r = 0$ and $c_r c_s$ as r_1 becomes large, according to equations 4.12 and 4.13, respectively. For this pack, statistical saturation occurs at approximately $l_c = 2(6) = 12$ mm, which is significantly smaller than the bounding box reported in Table 2.1, suggesting that the smaller bounding box is still large enough to provide a representative sample. Also notice that the two-point probability functions $S_{m,11}$ and $S_{11,m}$ exhibit identical behavior, as is also expected.

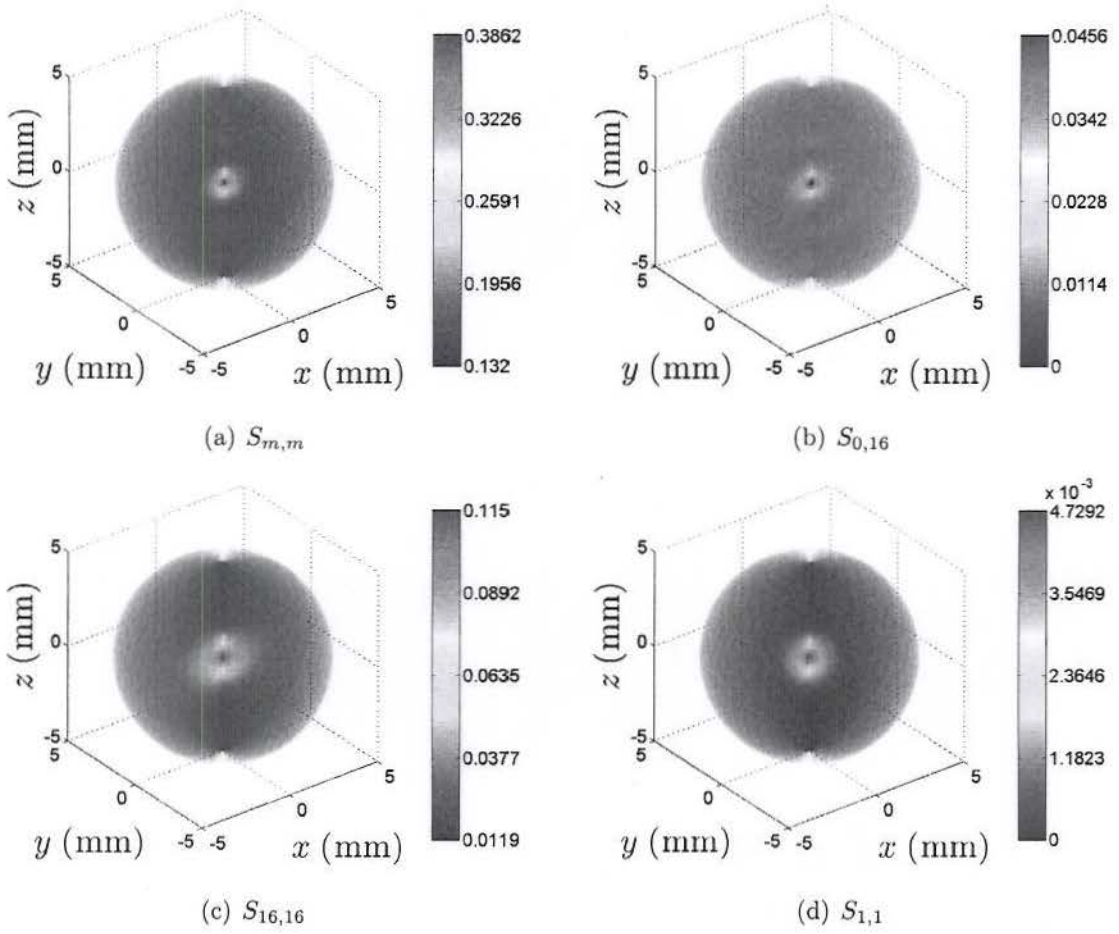

(a) $S_{m,m}$ (b) $S_{0,16}$

(c) $S_{16,16}$ (d) $S_{1,1}$

Figure 4.8. Selected complete two-point probability functions for the rice pack. Note that anisotropic behavior can be seen in the center of the probability functions, especially in (b) and (c). This reflects the parallelity observed in the pack which is quantified in figure 4.10 and most prominent in eccentric particles such as those belonging to bin 16. The decreased prominence of this anisotropic signature in (d) is due to the fact that the particles from bin 1 are significantly less eccentric than those from bin 16.

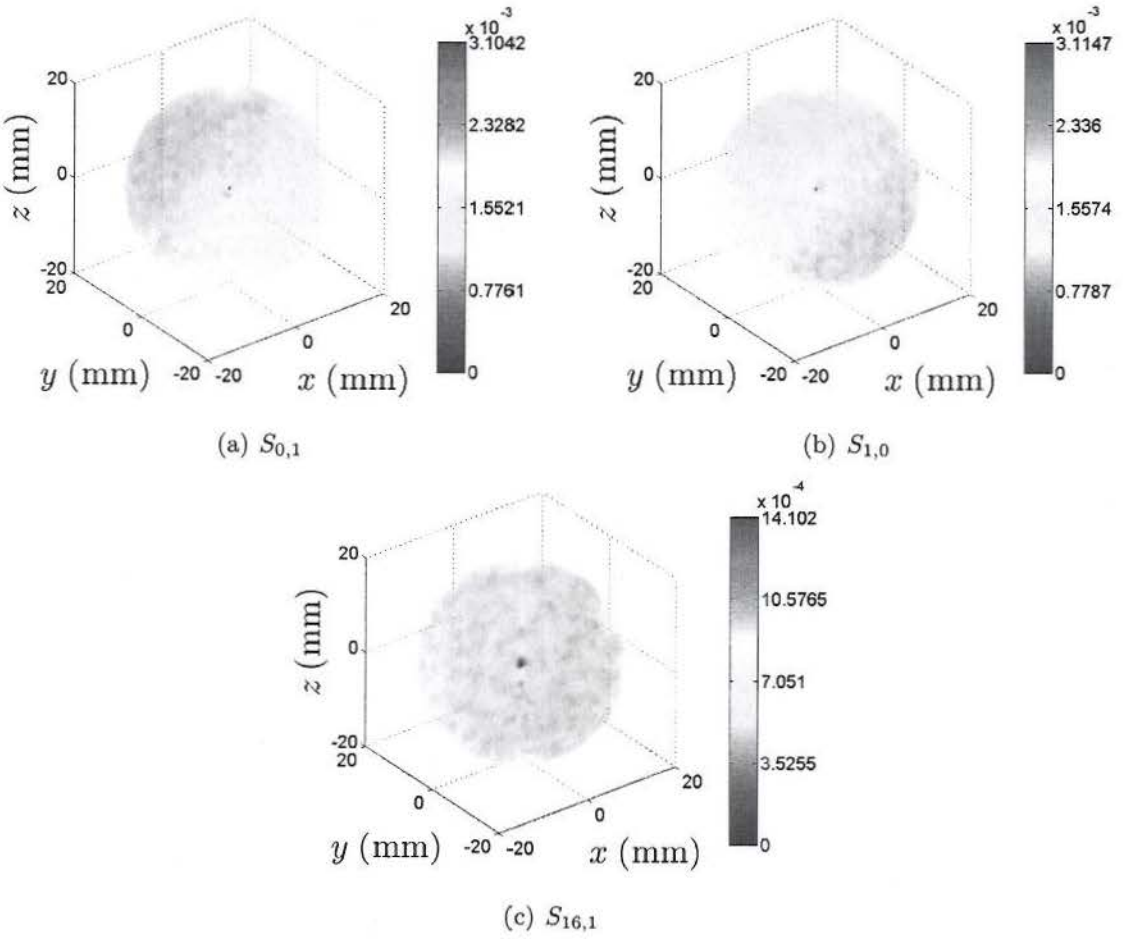

(a) $S_{0,1}$

(b) $S_{1,0}$

(c) $S_{16,1}$

Figure 4.9. Additional selected complete two-point probability functions for the rice pack. The highly anisotropic nature of these two-point probability functions is due to the more complex relations between the modes selected, demonstrating the need for a complete, anisotropic statistical analysis when greater detail in particle characterization is employed. Furthermore, (a) and (b) illustrate the symmetry described in equation 4.18.

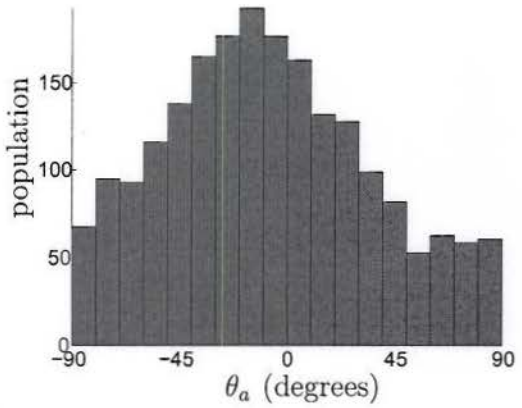

(a) The azimuthal orientation distribution of the particles.

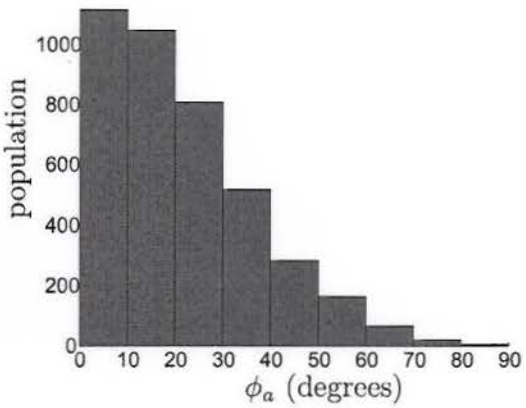

(b) The inclination orientation distribution of the particles.

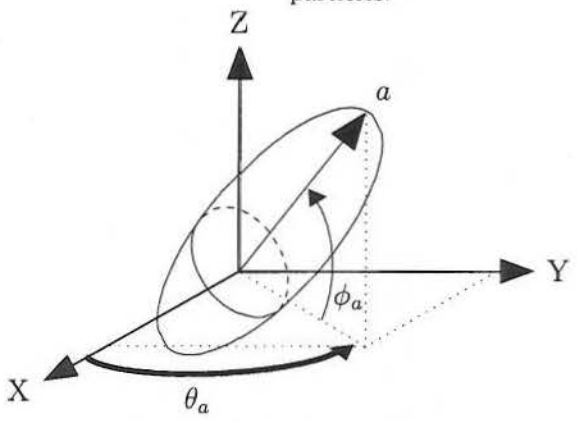

(c) Definitions of θ_a and ϕ_a.

Figure 4.10. The orientation distributions of ellipsoidal rice particles. Notice that the inclination angles, ϕ_a, of the ellipsoids tend towards 0°, which is concurrent with the observation that the particles tend to orient horizontally (see figure 3.16(c)), and the concentration of particles about $\theta_a = 15°$ is concurrent with the observation that the particles tend to exhibit parallelity in order to increase packing density (see figure 3.4(a)).

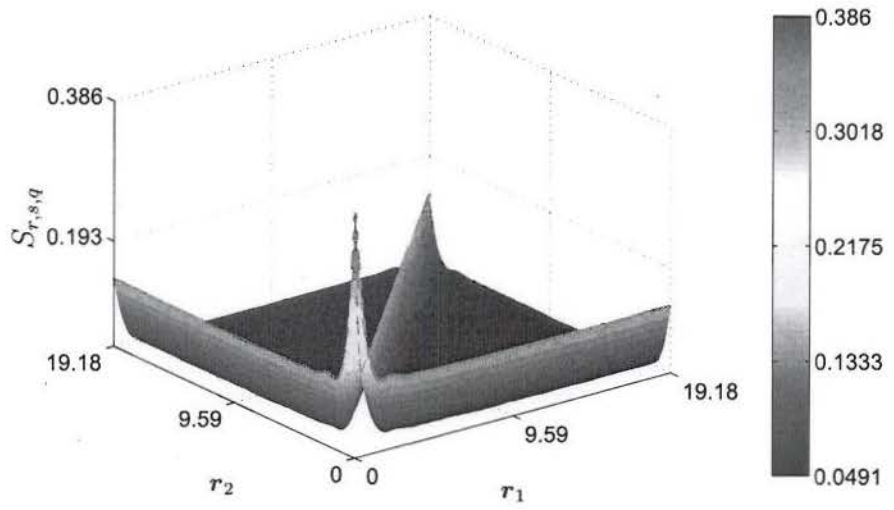

(a) $S_{m,m,m}$, $\theta = 0°$ with degenerate cases included

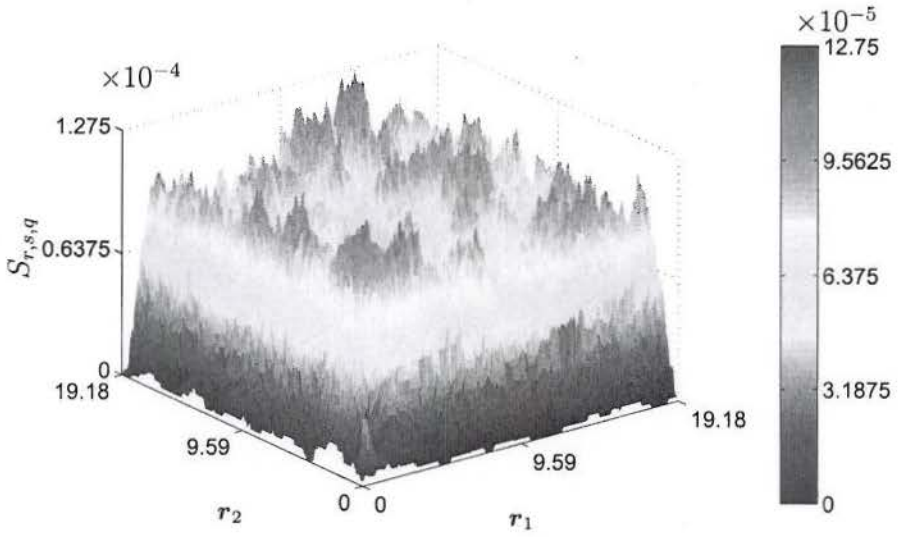

(b) $S_{1,16,16}$, $\theta = 180°$

Figure 4.11. Selected semi-isotropic three-point probability functions. Note that the subspace of the third-order probability function $S_{0,0,0}$ shown in (a) exhibits the degeneracies predicted by equations 4.14, 4.15, 4.17 (as long as $|\|\boldsymbol{r}_1\| - \|\boldsymbol{r}_2\||$ is sufficiently large), and 4.16. Moreover, (b) describes the probability of finding a small particle in between two large particles. The complex nature of this subspace of the $S_{1,16,16}$ probability function demonstrates that, as was the case with many complete two-point probability functions, the correlations between particle bins can be very complex.

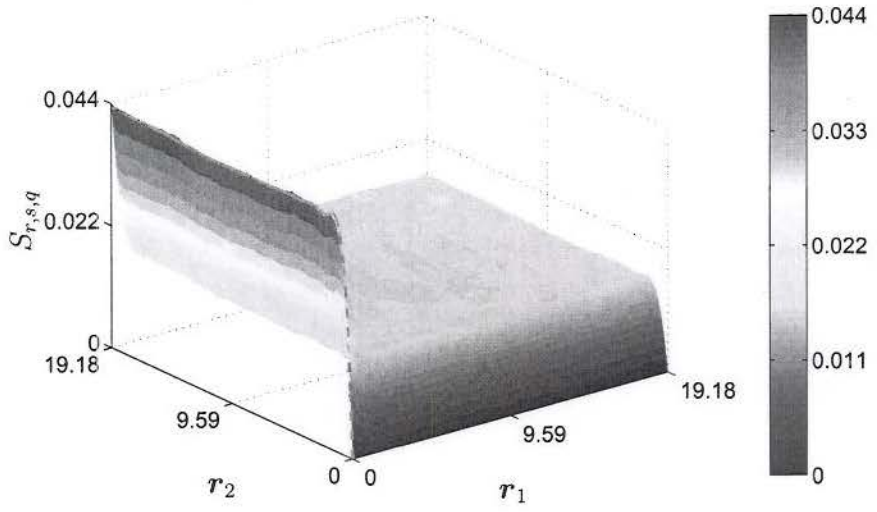

(a) $S_{m,m,16}$, $\theta = 90°$

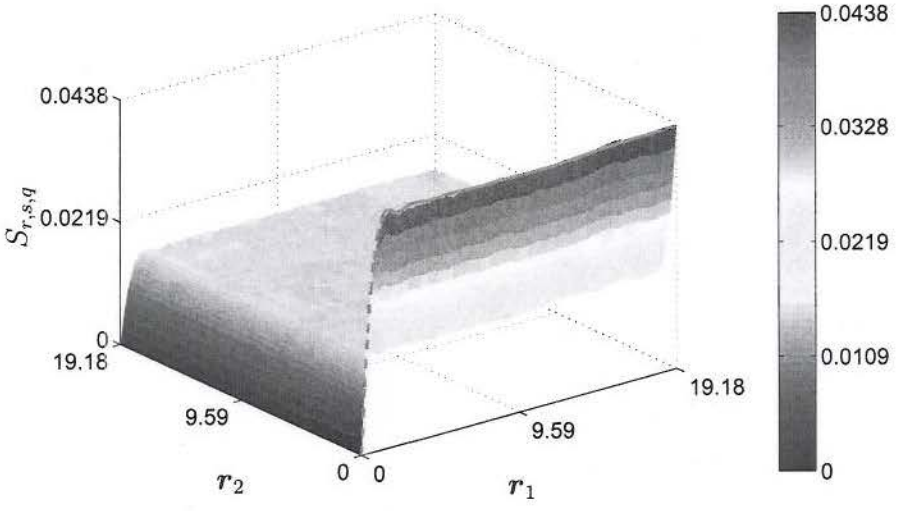

(b) $S_{m,16,m}$, $\theta = 90°$

Figure 4.12. A demonstration of the transpose symmetry described in equation 4.19.

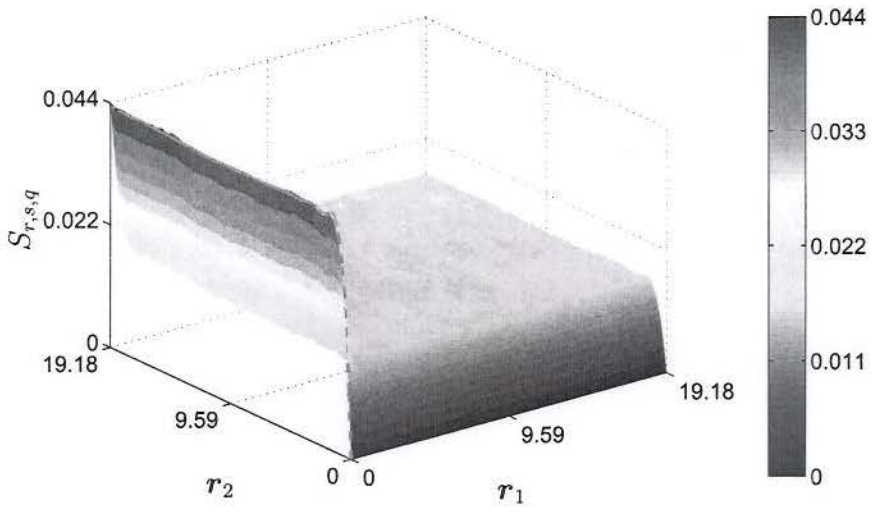

(a) $S_{m,m,16},\ \theta = 90°$

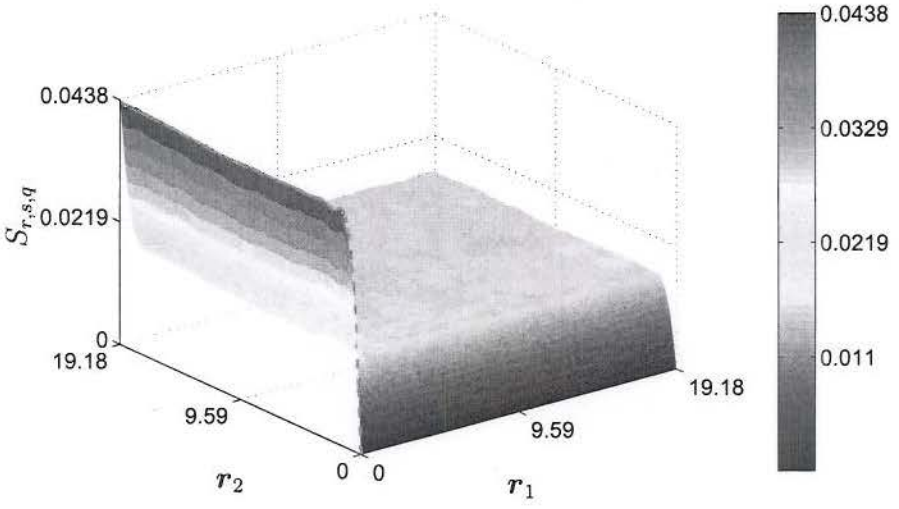

(b) $S_{m,m,16},\ \theta = 270°$

Figure 4.13. A demonstration of the angle identity described in equation 4.21.

CHAPTER 5

Polydisperse Particulate Media

After the algorithms for shape reduction, binning, and statistical analysis were developed, several mixtures of long-grain white rice and black mustard seeds were analyzed. Figure 5.1 shows the total volume fraction of four different mixtures of rice and mustard (described in tables 2.1, 5.1, 7.1, and 7.2), and Figure 5.2 shows volume fractions as they apply to the rice and mustard modes separately. Notice that the mixture of 25 % wt mustard has a significantly lower volume fraction. By looking at Figure 5.3, one may readily see that significant void space occurs where rice and mustard particles meet, possibly due to a size ratio between the two which is not conducive to efficient packing. The mixture of 25 % wt mustard and 75 % wt rice is characterized in depth in what follows in order to illustrate the complexities of the bimodal system and its treatment from the methods that have been explained.

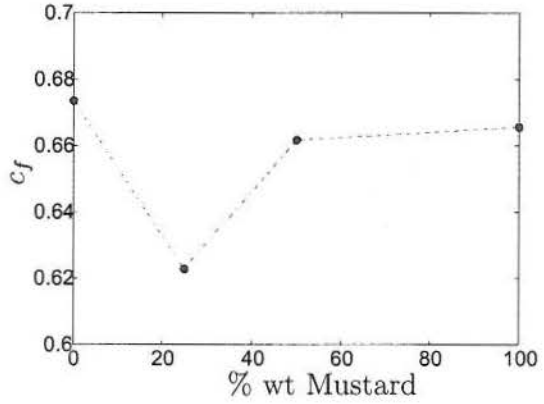

Figure 5.1. Volume fractions associated with various close-packed mixtures of rice and mustard. The data sets used are described in tables 2.1, 5.1, 7.1, and 7.2. Notice that the volume fraction decreases when ellipsoidal and spherical particles are mixed. This is concurrent with the qualitative observation that the different particle modes chosen do not mix well and introduce jamming.

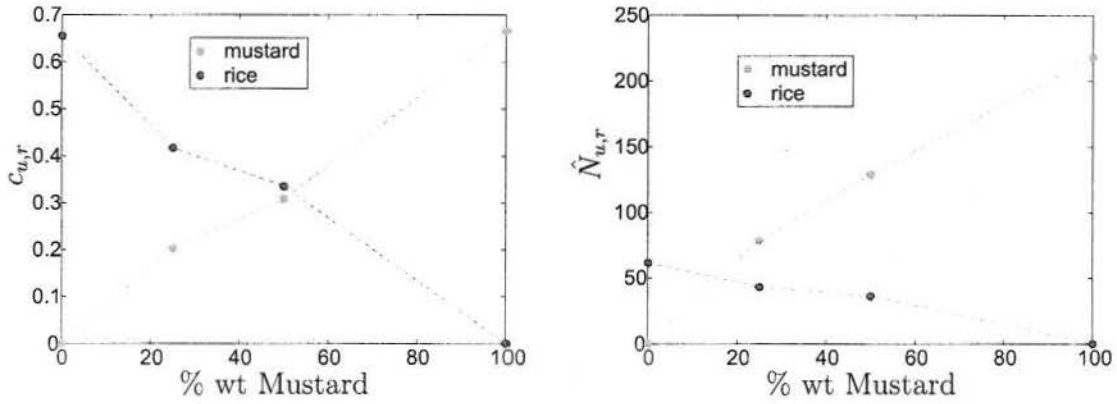

(a) Volume fractions of the two modes.

(b) Number of particles per cubic centimeter by mode.

Figure 5.2. Trends in component particle volume fractions of rice and mustard (c_r and c_u, respectively) and number of particles per cubic centimeter, $\hat{N}_{u,r}$, for individual modes in the various mixtures. The component behavior of the matrix (air) is ommitted, though it may be noted that $c_u + c_r + c_a = 1$, where c_a is the volume fraction of air. As is expected, (a) demonstrates how the mass fractions of each particluate component are closely related to their component volume fractions. However, because the mustard seeds have a smaller per-particle volume than rice, the number of mustard particles in the mixture increases relatively quickly as the mass fraction of mustard increases.

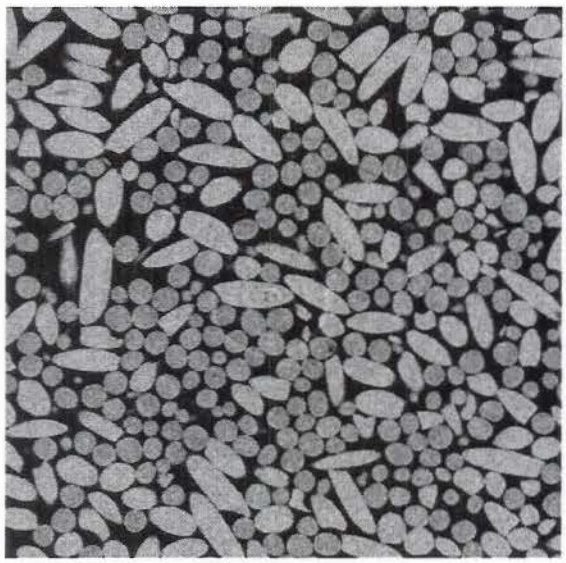

Figure 5.3. A sample grayscale cross-section of the voxel pack of the 25 % wt mustard mixture. Notice how extra void space is present near the areas where rice and mustard particles interact.

5.1 Example Pack

A specimen was prepared by mixing 90.004 g rice and 30.000 g black mustard. The two components were weighed separately then combined into a single container and shaken until they were evenly mixed. The mixture was then poured into the cannister shown in Figure 2.1 and preparation continued as outlined in section 2.1. The mixture was then scanned at 100 kV and 10 W, and a three-dimensional voxel image was constructed and post-processed according to the procedure outlined in section 2.3. The resulting voxel pack is shown in Figure 5.4. Properties of interest for the voxel pack are tabulated in table 5.1.

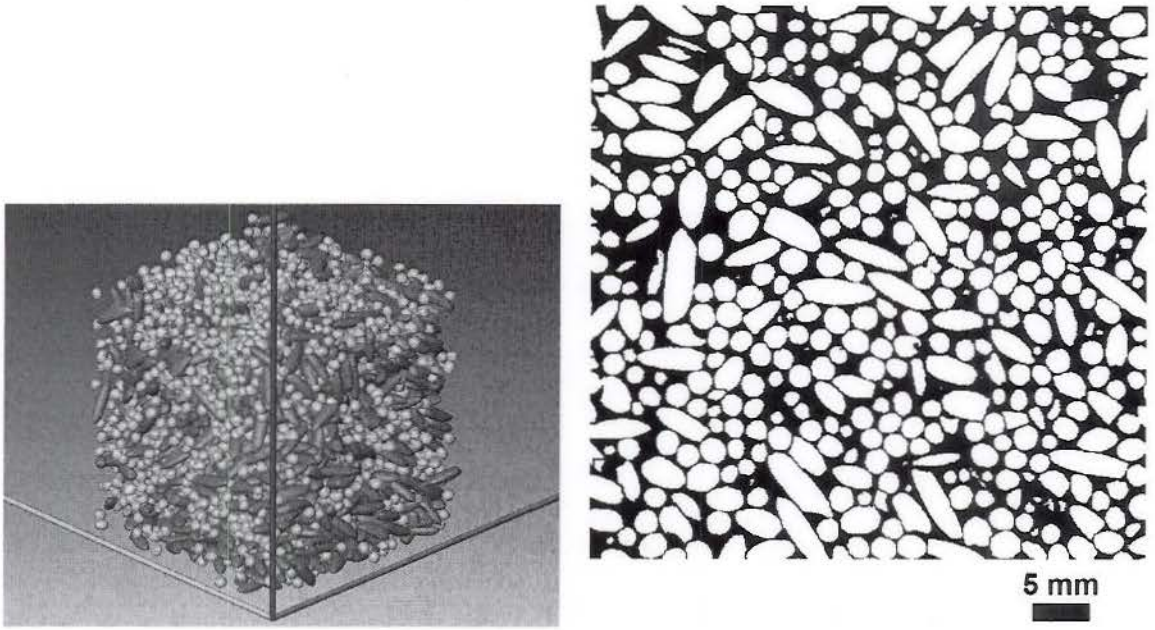

(a) The voxel pack. (b) A sample filtered cross-section of the voxel pack.

Figure 5.4. The voxel pack for the example polydisperse pack. The pack contains 6011 particles (1857 rice, 4154 mustard). Modes are identified by color; the yellow particles are mustard, and the blue particles are rice.

It can be seen from Figure 5.3 that the mustard and rice particles may be qualitatively distinguished from each other on the basis of shape (the mustard appears much more regular, and the rice appears to be more eccentric) and by average grayscale value (mustard appears darker than rice). Note also that there is a distribution of grayscale values over which rice

Table 5.1

Scan data and image processing data for the example polydisperse pack

Pixel Size	69.40	μm / pixel
Volume of interest	589 × 589 × 596	pixel^3
	2.07×10^8	voxels
	4.09 × 4.09 × 4.14	cm^3
	69.3	cm^3
Volume fraction before separation	0.6220	
Volume fraction after separation	0.6190	
Percent of volume remaining	99.5	%
Decrease in overall volume fraction	0.0029	
Number of particles before boundary layer removal	8420	
Number of particles after boundary layer removal	6011	
Number of rice particles	1857	
Number of mustard particles	4154	
Volume fraction of rice	0.4175	
Volume fraction of mustard seed	0.2015	

and mustard particles lie. This distribution of values is a limiting factor in the number of distinct phases which my be detected using this technique, though if a greater difference were desired between the phases, the use of a contrast agent could help to accentuate the difference. In order to objectively differentiate the two modes, the average grayscale value of each particle $\overline{\rho_i}$ (defined for a given particle i) was determined, and a thresholding value was determined above which particles are assumed to be rice, and below which particles are assumed to be mustard. By considering figures 5.5(a) and 5.5(b), this value was determined to be $\overline{\rho}_i = 144.5$.

After analysis was carried out in *Amira*, the pack was converted into a representative ellipsoidal pack, shown in Figure 5.6. The errors associated with the ellipsoidal representation are shown in Figure 5.7 and tabulated in table 5.2. Note that, while the mean value of Π_2 is small, the maximum value is substantially higher. Again, this is because of problems with the separation algorithm, yielding groups of particles similar to that which is shown in

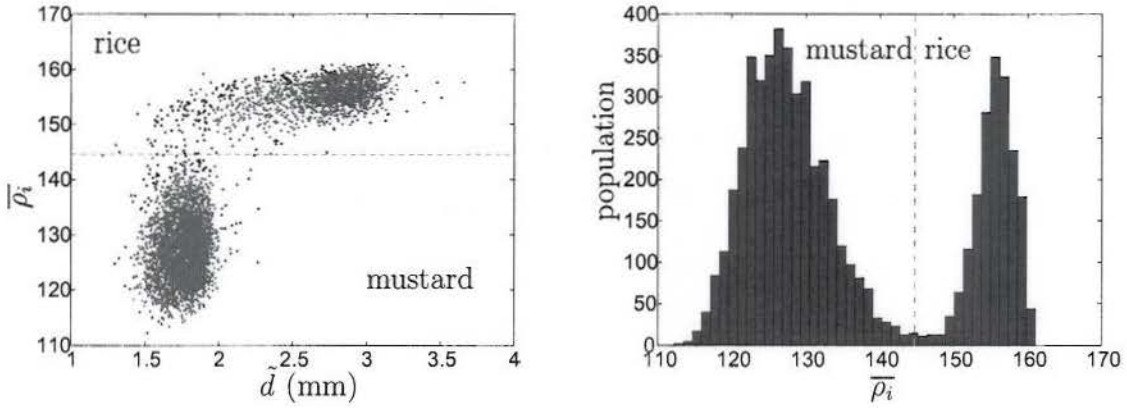

(a) Density plotted as a function of particle size. (b) The distribution of particles' mean grayscale value.

Figure 5.5. The density characteristics of particles in the pack. Notice that (b) shows two distinct peaks in terms of density, suggesting that rice and mustard may be differentiated from one another with respect to a density thresholding value. (a) shows that the density divide corresponds to a difference in size. A thresholding value of $\overline{\rho}_i = 144.5$ (shown by the red dashed line) separates the particles into two different groupings. It can then be inferred that the larger, denser particles are rice, and the smaller, less dense particles are mustard.

Figure 3.2.

Table 5.2

Errors in ellipsoidal reduction

	minimum	mean	maximum	< 5 %
ΔV	0.27 %	0.74 %	3.88 %	100 %
ΔS	1.57 %	4.76 %	40.49 %	74.11 %
Π_2	1.03×10^{-3} %	0.95 %	39.18 %	98.05 %

The binning routine was carried out to characterize the distribution of particles, and the resulting distributions are shown in Figure 5.8. The scatter of the particles is shown in Figure 5.9. Using the ellipsoidal representation and binning scheme, one-, two-, and three-point probability functions were computed numerically for the pack using *Stat3D*. Figure 5.10 shows the volume fractions of the pack as computed directly in the voxel pack and

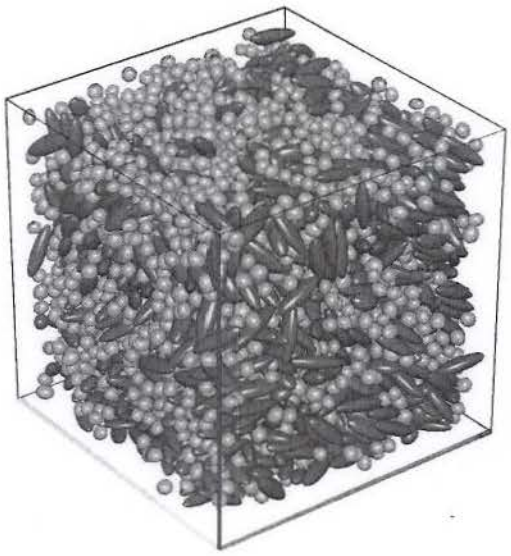

Figure 5.6. The representative ellipsoidal pack for the 75 % wt rice, 25 % wt black mustard pack. Particles are identified as either rice (purple) or mustard (yellow) based off of their average grayscale values. Notice that that individual particles may be traced back to their voxel pack equivalents in Figure 5.4(a).

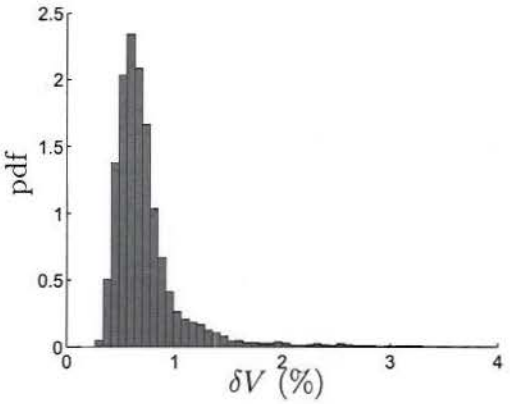

(a) The error in per-particle volume.

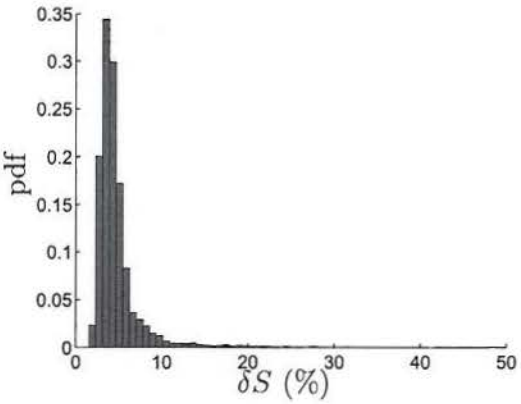

(b) The error in per-particle surface area.

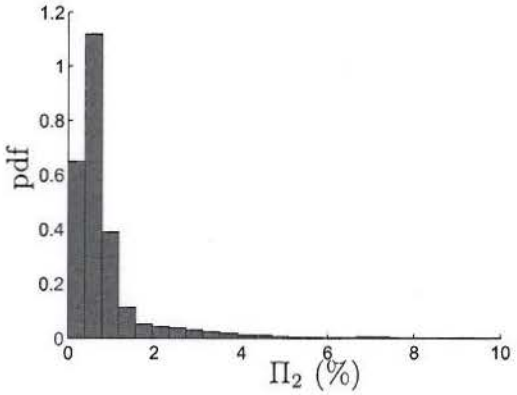

(c) The error in per-particle orientation.

Figure 5.7. The per-particle error in shape reduction in terms of volume (shown in (a)), surface area (shown in (b)), and orientation (shown in (c)). A weighting value of $\eta = 0.8$ was chosen in order to ensure an accurate match in terms of particle volume, allowing for limited input from the surface area of the particle to be matched.

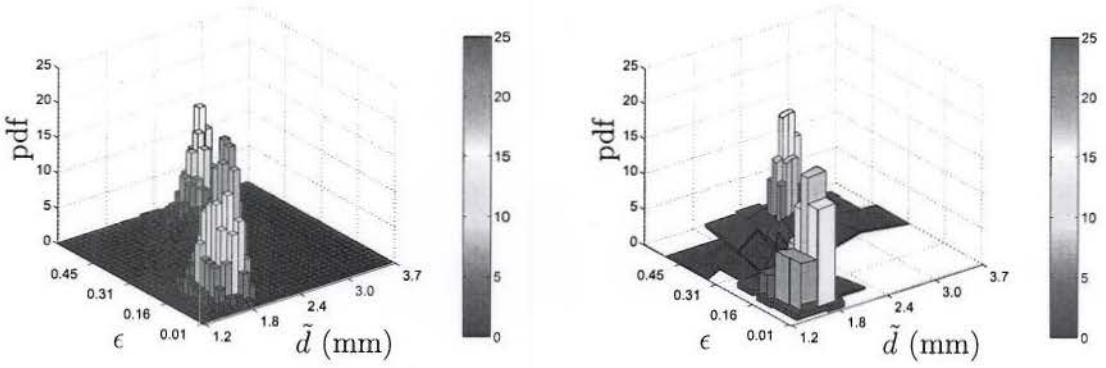

(a) The fine binning.

(b) The coarse binning.

Figure 5.8. The binning for the 75 % wt rice, 25 % wt black mustard pack. Notice that two different peaks are present in the particle distribution, corresponding to the black mustard (bottom-left) and rice (top-right). The coarse binning captures the distribution using 28 bins.

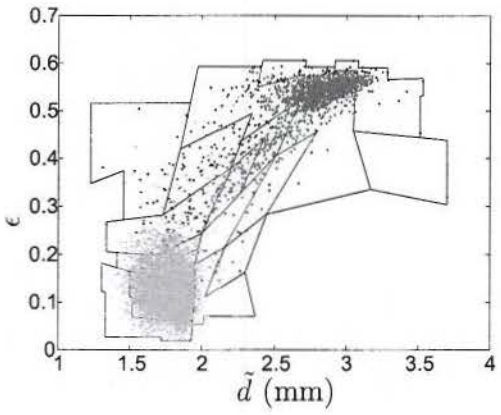

Figure 5.9. The distributions of particles for the example polydisperse pack. Mustard particles are shown as yellow points, and rice particles are shown as blue points.

through use of the one-point probability function. Figure 5.11 shows the numbering of the bins for reference. In addition, selected two- and three-point probability functions are shown in figures 5.12, 5.13, 5.14, and 5.15.

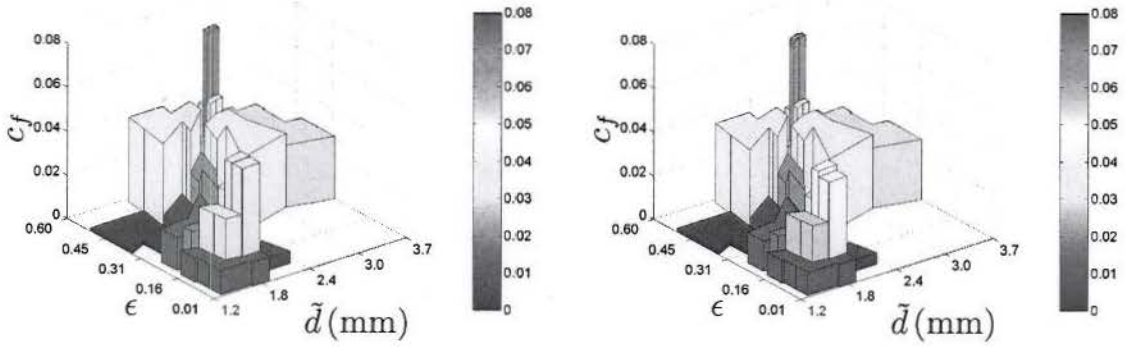

(a) Volume fractions of the voxel pack.

(b) Volume fractions of the ellipsoidal pack.

Figure 5.10. The volume fractions associated with the bins of the example polydisperse pack. (a) is computed directly from the voxel pack, and (b) was computed using the one-point probability functions associated with the various bins.

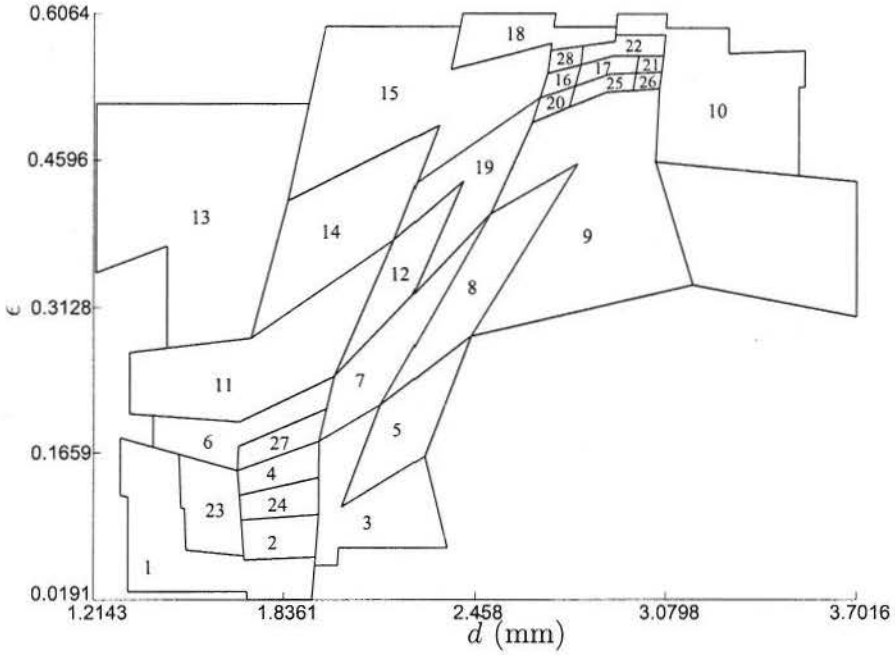

Figure 5.11. Indices associated with the coarse binning for the example polydisperse pack.

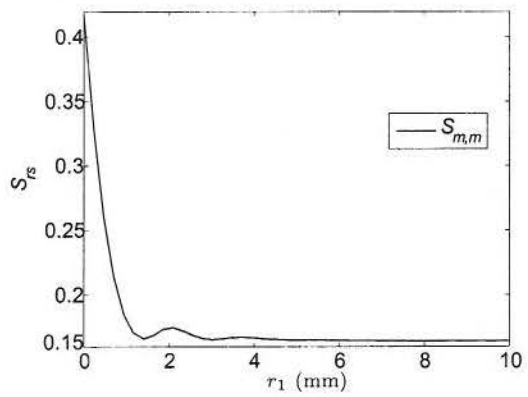

(a) Selected isotropic two-point probability functions.

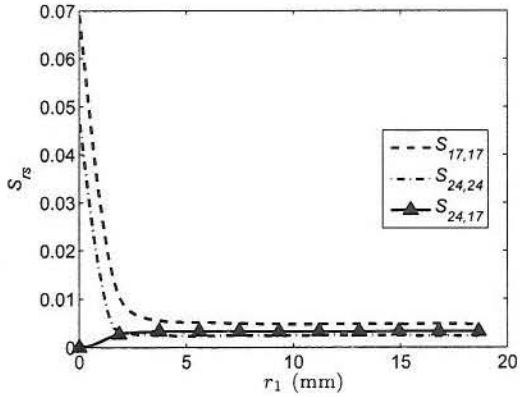

(b) Selected isotropic two-point probability functions (continued).

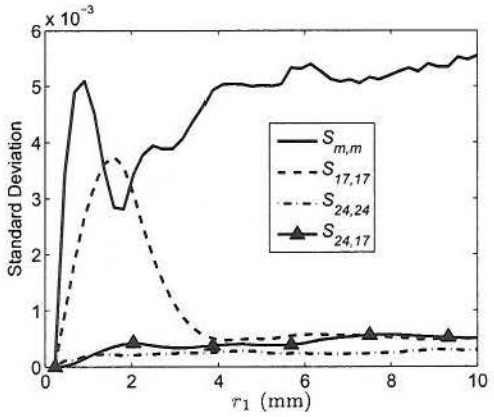

(c) Standard deviation of selected isotropic two-point probability functions.

Figure 5.12. Selected isotropic two-point probability functions for the example polydisperse pack.

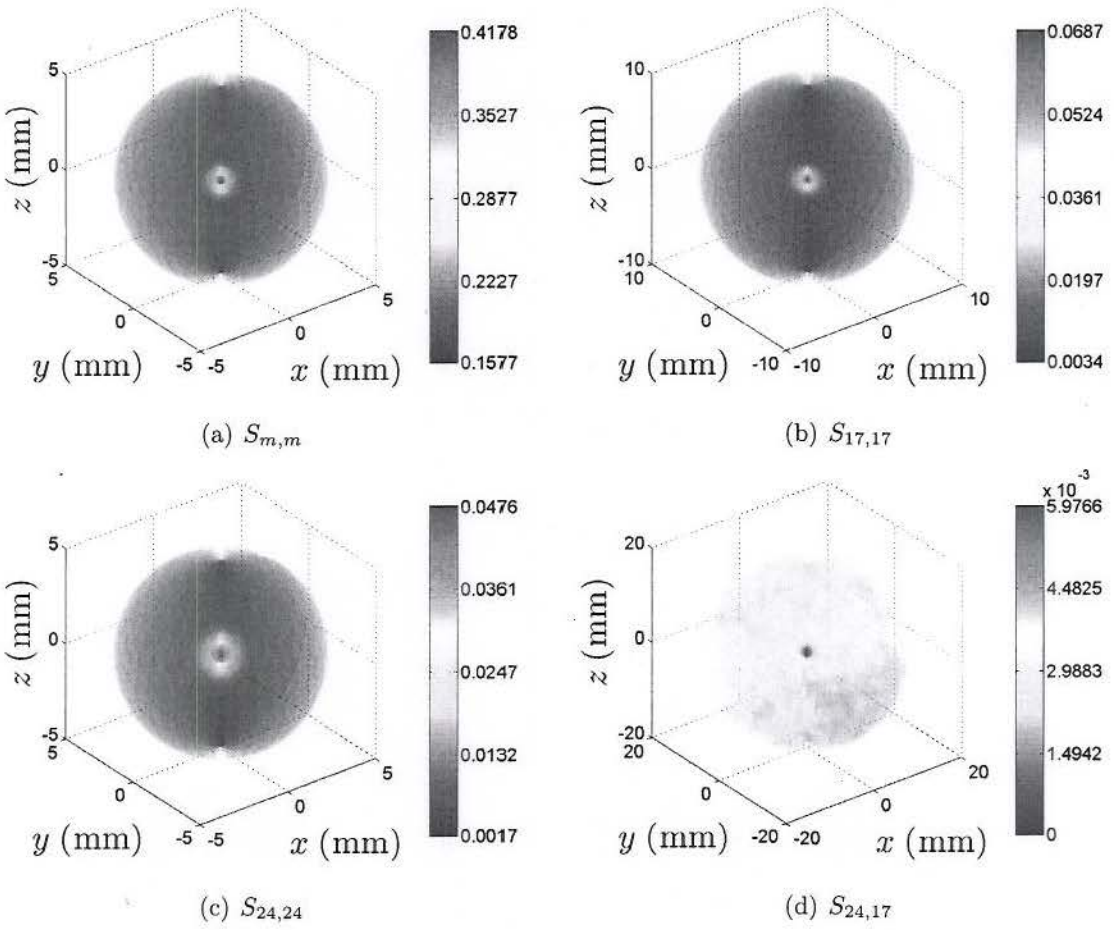

(a) $S_{m,m}$ (b) $S_{17,17}$

(c) $S_{24,24}$ (d) $S_{24,17}$

Figure 5.13. Selected complete two-point probability functions for the example polydisperse pack.

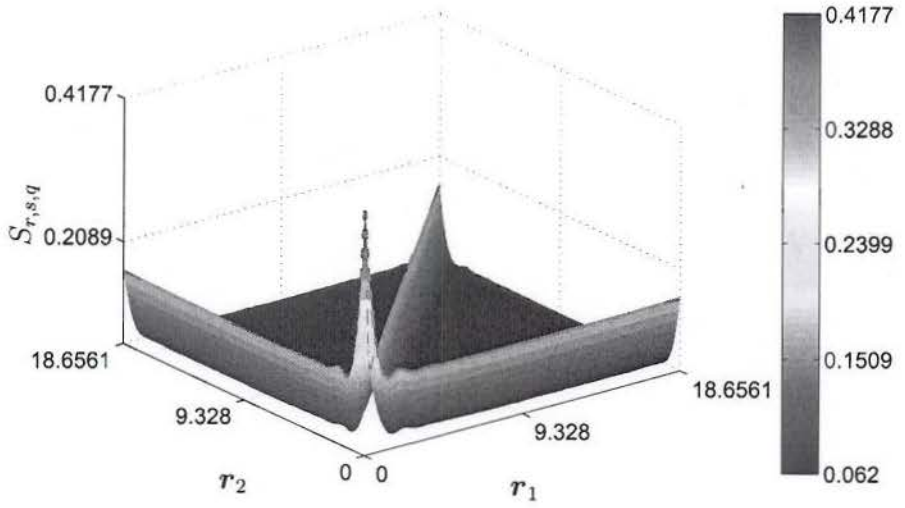

(a) $S_{m,m,m}$, $\theta = 0°$

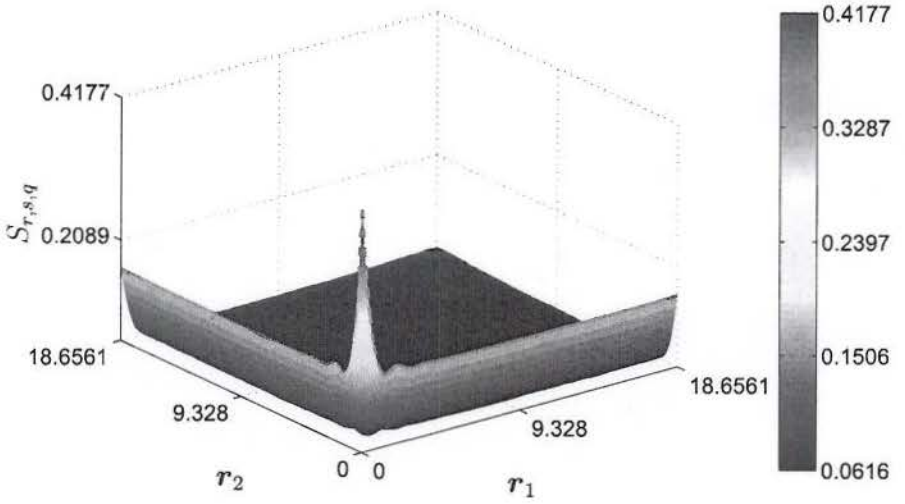

(b) $S_{m,m,m}$, $\theta = 180°$

Figure 5.14. Semi-isotropic three-point probability functions computed for the example polydisperse pack. Second-order degeneracies are plotted in red dashed lines for $r_1 = 0$, $r_2 = 0$, and $r_1 = r_2$ in (a) and for $r_1 = 0$ and $r_2 = 0$ in (b). Notice that the degenerate case described in equation 4.16 is present in (a) but disappears in (b) because $\theta_{rsq} \neq 0$. Otherwise, the degenerate cases described in equations 4.14, 4.15, and 4.17 are all present in both plots.

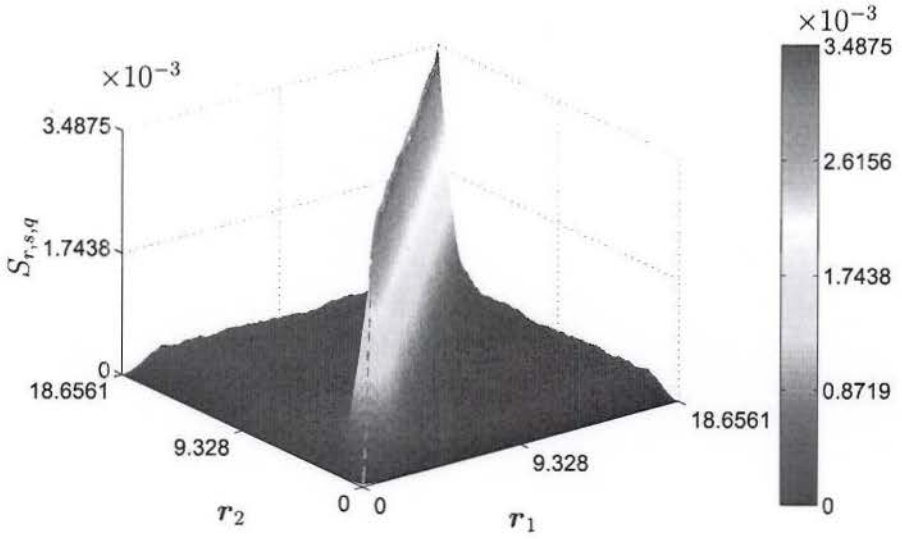

(a) $S_{24,17,17}$, $\theta = 0°$

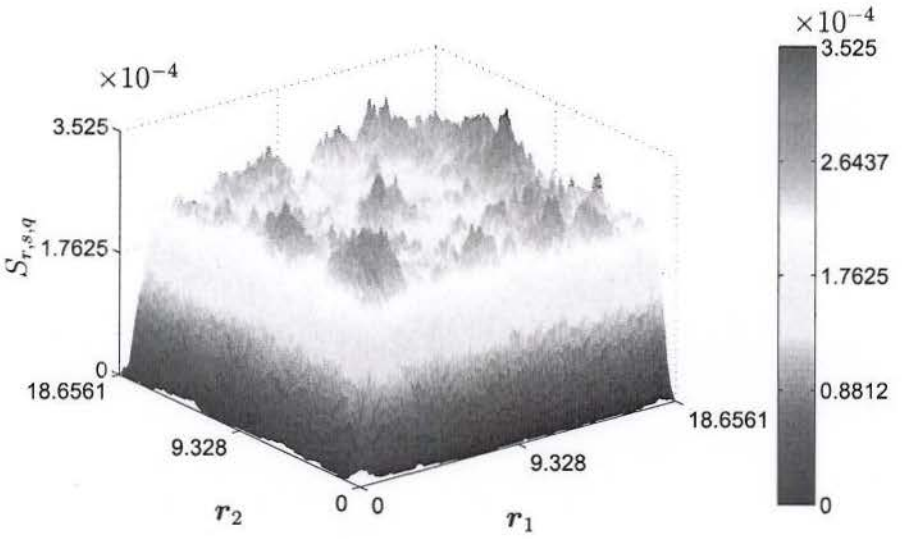

(b) $S_{24,17,17}$, $\theta = 90°$

Figure 5.15. Semi-isotropic three-point probability functions computed for the example polydisperse pack. The second-order degeneracy for $\boldsymbol{r}_1 = \boldsymbol{r}_2$ is plotted as a dashed red line in (a). Notice that the degenerate case described in equation 4.16 is present in (a) but disappears in (b) because $\theta_{rsq} \neq 0$. Otherwise, the degenerate cases described in equations 4.14, 4.15, and 4.17 are all present in both plots.

CHAPTER 6

Conclusions and Future Work

The goal of this work was to develop methods to characterize the packing behavior of polydisperse particulate packs. First, microtomography was used in order to obtain experimental data on heterogeneous specimens, and three-dimensional voxel packs were constructed using commercial software. Geometrical information was computed on a per-particle basis for the inclusions in the voxel pack and used to construct a representative pack using ellipsoids or cuboids.

A method was developed which inputs the geometrical information from the voxel pack and generates a representative pack using ellipsoids or cuboids. From these representative particles, information about the distribution of particle shapes and sizes was quantified using geometric metrics. A routine was developed which creates a two-dimensional coarse binning that captures the probability distribution of the particles based on these metrics. Several steps were devised and implemented to capture the characteristics of the distribution using significantly fewer bins than are needed with a uniform, fine binning. Particles were then classified based on which bin they belong to.

A statistical investigation of the representative pack was carried out using the binning to enhance the specificity of the modes referenced by the n-point probability functions. *Stat3D* was advanced to analyze ellipsoidal particles, and the routine for computing three-point probability functions was rewritten using the semi-isotropic assumption *a priori* in order to increase the efficiency of the third-order analysis. The statistical analysis was performed in a parallel computing environment.

After the functionality of the above developments was demonstrated on a monodisperse packing of rice, various polydisperse mixtures of rice and mustard were analyzed. The results of these analyses indicate that the methods developed are effective tools for analyzing polydisperse particulate systems.

In the future, statistical analysis may be carried out directly on the voxel data. This would serve to validate the findings of statistical analyses on packs of representative, idealized shapes. Moreover, the statistical data about the morphology of the particulate packs may be used to either inform the creation of a statistically-identical representative unit cell on which properties may be directly solved, or they may be used in tandem with the properties of individual inclusions as part of a variational method such as the Hashin-Shtrikman variational principles to compute mechanical and transport properties of particulate systems [20, 28, 29]. In addition, work can be done to develop a more extensive library of three-dimensional shapes which may be used to represent crystal-like inclusions in a pack, enabling the representative pack to better approximate a greater variety of particulate composites.

Acknowledgments

The author would like to gratefully acknowledge the support from the Alliant Techsystems Inc., Dr. I. L. Davis - program manager (ATK-62156). The author would like to also acknowledge the support from IllinoisRocstar LLC under the contract numbers FA9300-10-C-3003 (Edwards Air Force Base, SBIR Phase II project) and FA8651-10-M-0256 (Eglin Air Force Base, SBIR Phase I project) by the Office of the secretary of defense as a part of the Phase II and Phase I SBIR programs.

Any opinions, findings and conclusions or recommendations expressed in this material are those of the author(s) and do not necessarily reflect the views of the Alliant Techsystems Inc., IllinoisRocstar LLC and the U.S. Air Force.

CHAPTER 7

Appendix

The scan data for the other packs which were referenced in chapter 5 are included here.

Table 7.1

Scan data and image processing data for the 60.001 g (50 % wt) mustard, 60.002 g (50 % wt) rice pack.

Pixel Size	69.40	μm / pixel
Volume of interest	$595 \times 595 \times 566$	pixel^3
	2.03×10^8	voxels
	$3.86 \times 3.86 \times 3.93$	cm^3
	66.98	cm^3
Volume fraction before separation	0.6573	
Volume fraction after separation	0.6429	
Percent of volume remaining	97.80	%
Decrease in overall volume fraction	0.0144	
Number of particles before boundary layer removal	11067	
Number of particles after boundary layer removal	7766	
Number of rice particles	1599	
Number of mustard particles	6167	
Volume fraction of rice	0.3353	
Volume fraction of mustard seed	0.3076	

Table 7.2

Scan data and image processing data for the 100 % wt mustard, 0 % wt rice pack.

Pixel Size	69.40	μm / pixel
Volume of interest	$589 \times 589 \times 566$	pixel^3
	1.96×10^8	voxels
	$4.09 \times 4.09 \times 3.93$	cm^3
	65.63	cm^3
Volume fraction before separation	0.6964	
Volume fraction after separation	0.6606	
Percent of volume remaining	94.86	%
Decrease in overall volume fraction	0.0358	
Number of particles before boundary layer removal	14313	
Number of particles after boundary layer removal	11117	
Number of rice particles	0	
Number of mustard particles	11117	
Volume fraction of rice	0	
Volume fraction of mustard seed	0.6606	

BIBLIOGRAPHY

[1] M. J. Beran. *Statistical Continuum Theories.* Interscience, 1968.

[2] S. Torquato. *Random Heterogeneous Materials: Microstructure and Macroscopic Properties.* Springer, 2002.

[3] L-N. Zou, X. Cheng, M. L. Rivers, H. M. Jaeger, and S. R. Nagel. The packing of granular polymer chains. *Science*, 326(408), 2009.

[4] P. M. Chaikin and T. C. Lubensky. *Principles of Condensed Matter Physics.* Cambridge University Press, 2000.

[5] T. Ding, K. Song, K. Clays, and C.-H. Tung. Controlled directionality of elipsoids in monolayter and multilayer colloidal crystals. *Langmuir*, 26:11544–11549, 2010.

[6] J. S. Kahn. The analysis and distribution of the properties of packing in sand-size sediments: 1. on the measurement of packing in sandstones. *J. Geol.*, 64(4):385–395, 1956.

[7] D. A. Weitz. Packing in the spheres. *Science*, 303(968), 2004.

[8] P. M. Chaikin, A. Donev, W. Man, F. H. Stillinger, and S. Torquato. Some observations on the random packing of hard ellipsoids. *Ind. Eng. Chem. Res.*, 45:6960–6965, 2006.

[9] A. Donev, I. Cisse, D. Sachs, E. A. Variano, F. H. Stillinger, R. Connelly, S. Torquato, and P. M. Chaikin. Improving the density of jammed disordered packings using ellipsoids. *Science*, 303:990–993, 2004.

[10] P. A. Smith and R. A. Haber. Effect of particle packing on the filtration and rheology behavior of extended size distribution alumina suspensions. *J. Am. Chem. Soc.*, 78:1737–1744, 1995.

[11] S. Torquato, T. M. Truskett, and P. G. Debenedetti. Is random close packing of spheres well defined? *Phys. Rev. Lett.*, 84(10):2064–2067, 2000.

[12] W. S. Jodrey and E. M. Tory. Computer simulation of close random packing of equal spheres. *Phys. Rev. A*, 32(4):2347–2351.

[13] A. S. Clarke and J. D. Wiley. Numerical simulation of the dense random packing of a binary mixture of hard spheres: Amorphous metals. *Phys. Rev. B*, 35(14):7350–7356.

[14] A. Bezrukov and D. Stoyan. Simulation and statistical analysis of random packings of ellipsoids. *Part. Part. Syst. Charact.*, 23:388–398, 2006.

[15] S. Torquato and Y. Jiao. Dense packings of the platonic and archimedean solids. *Nature*, 460:876–879, 2009.

[16] G. M. Knott, T. L. Jackson, and J. Buckmaster. The random packing of heterogeneous propellants. *AIAA J.*, 39:678–686.

[17] B. P. Flannery, H. W. Deckman, W. G. Roberge, and K. L. D'Amico. Three-dimensional x-ray microtomography. *Science*, 237(4821):1439–1444, 1987.

[18] H. Lee, M. Brandyberry, A. Tudor, and K. Matouš. Three-dimensional reconstruction of statistically optimal unit cells of polydisperse particulate composites from microtomography. *Phys. Rev. E*, 80(6), 2009.

[19] B. C. Collins, K. Matouš, and D. Rypl. Three-dimensional reconstruction of statistically optimal unit cells of multimodal particulate composites. *Int. J. Multiscale Comp. Eng*, 8(5):489–507, 2010.

[20] H. Lee, A. S. Gillman, and K. Matouš. Computing overall elastic constants of polydisperse particulate composites from microtomographic data. *J. Mech. Phys. Solids.* Submitted for publication.

[21] K. E. Thompson, C. S. Willson, and W. Zhang. Quantitative computer reconstruction of particulate materials from microtomography images. *Powder Technology*, 163:169–182, 2006.

[22] Quantitative measurements of localized density variations in cylindrical tablets using x-ray microtomography. *European Journal of Pharmaceutics and Biopharmaceutics*, 64(1):38 – 50, 2006.

[23] Skyscan NV. *NRecon User Manual.* 2011.

[24] Visage Imaging. *Amira 5 Reference Guide.* 2010.

[25] Noesis. *Visilog 6 Reference Guide.* 2010.

[26] Surface area estimation of digitized 3d objects using weighted local configurations. *Image Vision Comput*, 23(2):111 – 122, 2005.

[27] M. S. Klamkin. Elementary approximations to the area of n-dimensional ellipsoids. *Am. Math. Mon.*, 78(3):280–283, 1971.

[28] Z. Hashin and S. Shtrikman. A variational approach to the theory of the elastic behaviour of multiphase materials. *J. Mech. Phys. Solids*, 11:127–140, 1963.

[29] J. R. Willis. Bounds and self-consistent estimates for the overall properties of anisotropic composites. *J. Mech. Phys. Solids*, 25:185–202, 1977.